

# The Reaction Mechanism of Bovine Lens Leucine Aminopeptidase

Gudrun Schürer,<sup>†</sup> Anselm H. C. Horn,<sup>†</sup> Peter Gedeck,<sup>‡</sup> and Timothy Clark<sup>\*,†</sup>

Computer-Chemie-Centrum, Friedrich-Alexander-Universität Erlangen-Nürnberg,  
Nägelsbachstrasse 25, 91052 Erlangen, Germany, and Novartis Horsham Research Centre,  
Wimblehurst Road, Horsham, West Sussex RH12 5AB, U.K.

Received: January 29, 2002; In Final Form: May 31, 2002

We present a quantum mechanical/molecular mechanical (QM/MM) study using the AM1 Hamiltonian and a flexible MM part on the mode of action of the bovine lens leucine aminopeptidase (bLAP), a cytosolic exopeptidase that catalyzes the cleavage of the N-terminal amide bond of peptides. The reaction mechanism of this ubiquitous enzyme has not yet been clarified completely, although some suggestions based on crystallographic data have been made. One path of the several possibilities investigated was found to be clearly the most favorable and in good agreement with experimental results. Besides the elucidation of the functional roles of active-site residues, an estimation of the environment effects is given.

## Introduction

The exopeptidase bovine lens leucine aminopeptidase (bLAP, EC 3.4.11.1), a cytosolic enzyme, catalyzes the cleavage of amino acids from the N-termini of peptides. Aminopeptidases<sup>1</sup> are ubiquitous enzymes that play a key role in the modification, degradation, and metabolism of peptides. Alterations in aminopeptidase activity have been associated with a variety of pathological disorders such as cancer<sup>2</sup> and cataracts.<sup>3</sup> An increase of leucine aminopeptidase activity was observed in HIV-infected cells, and it has been suggested that the enzyme plays an important role in the early events of HIV infection, such as viral entry.<sup>4</sup> The reaction mechanisms of these enzymes are clearly crucial for understanding their modes of action but have not been identified uniquely by experimental studies.

Several 3D structures of the free enzyme and transition-state-analogue complexes are available in the Protein Data Bank<sup>5</sup> under the entries 1LAP,<sup>6</sup> 1BPN,<sup>7</sup> 1BPM<sup>8</sup> (Mg-bLAP), 1LAM,<sup>8</sup> 1BLL<sup>9</sup> (complexed with amastatin), 1LAN<sup>8</sup> (complexed with L-leucinal) and 1LCP<sup>10</sup> (complexed with L-leucine-phosphonic acid).

bLAP is a homohexameric enzyme with a molecular weight of 324 kDa that requires two Zn<sup>2+</sup> ions per subunit for catalytic activity. These are located in the active site (Figure 1) about 3.0 Å from each other. Such binuclear metal centers are also found in other hydrolases, such as bacterial aminopeptidases, carboxypeptidase G2, and metallo- $\beta$ -lactamase.<sup>11</sup> The metal-binding sites show different kinetics and affinities toward divalent metal ions. Zn488, which can be substituted by Mn<sup>2+</sup>, Mg<sup>2+</sup>, and Co<sup>2+</sup> ions, occupies the so-called *readily exchangeable site*. Zn489, located in the so-called *tight-binding site*, can be substituted by Co<sup>2+</sup> ions. In this case, the Zn<sup>2+</sup> ion can only be replaced via the structure in which both binding sites are unoccupied.<sup>7</sup>

The 3D-structures of the enzyme–inhibitor complexes show Zn488 to be coordinated to Asp255–O $\delta$ 2, Asp332–O $\delta$ 1, the backbone carbonyl oxygen of Asp332 (O<sub>backbone</sub>), which is a weak ligand, and Glu334–O $\epsilon$ 1. The Zn489 ligands are Lys250–

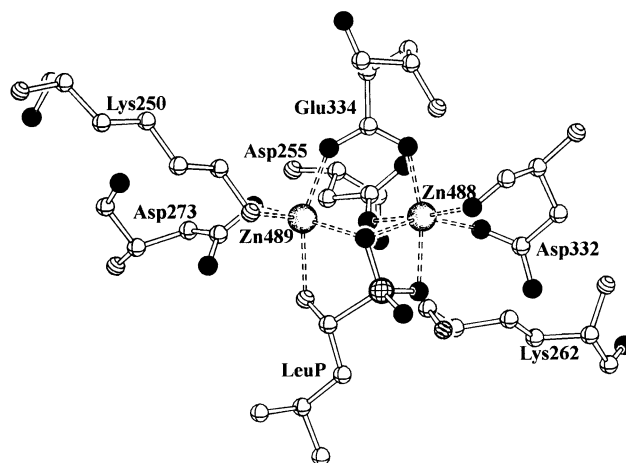
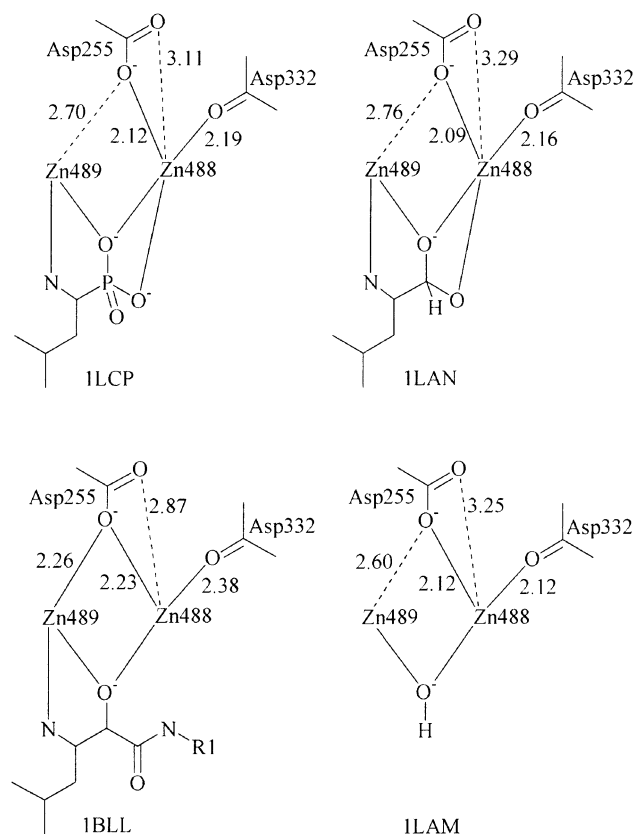


Figure 1. Active site of the bLAP–LeuP complex (PDB entry 1LCP).

N $\zeta$ , Asp273–O $\delta$ 2 and Glu344–O $\delta$ 2. In 1LCP, L-leucine-phosphonic acid (LeuP) is coordinated to Zn489 via its amino group and one phosphonate oxygen that acts as a bridging ligand between the two metal ions. At the same time, another phosphonate oxygen is coordinated to Zn488. Additionally, the N-terminal amino group of the inhibitor forms a hydrogen bond to Asp273–O $\delta$ 1. The coordination numbers are therefore 6 for Zn488 and 5 for Zn489, although the assignment of coordination numbers is somewhat arbitrary. For example, the distances between Zn488 and the backbone carbonyl oxygen of Asp332 and between Zn489 and Asp255–O $\delta$ 2 vary significantly in the enzyme–inhibitor complexes 1LCP, 1LAN, 1BLL, and the free enzyme 1LAM (see Figure 2). In 1LCP and 1LAN, the coordination number of Zn489 is 5 (in 1LAM 4), but the Zn489–Asp255–O $\delta$ 2 distance is only 2.70, 2.76, or 2.60 Å, respectively, indicating a weak interaction in addition to the five ligands in the first coordination sphere. In 1BLL, this distance is decreased to 2.26 Å, raising the Zn489 coordination number to 6. Because the tetrahedral group of the amastatin inhibitor has no geminal oxygens, it acts as a bridging ligand but occupies no further coordination site at Zn488, which thus has a coordination number of 5. However, Asp255–O $\delta$ 1 is

<sup>†</sup> Friedrich-Alexander-Universität Erlangen-Nürnberg.

<sup>‡</sup> Novartis Horsham Research Centre.



**Figure 2.** Asp255— and Asp332—O<sub>backbone</sub> binding modes of the enzyme—inhibitor complexes 1LCP (with L-leucine-phosphonic acid), 1LAN (with L-leucinal), and 1BLL (with amastatin) and of 1LAM (the free enzyme). The ligands Asp332—O $\delta$ 1 and Glu334—O $\delta$ 1 (bound to Zn488), as well as Lys250—N $\zeta$ , Asp273—O $\delta$ 2, and Glu334—O $\delta$ 2 (bound to Zn489), are not shown.

positioned within interaction distance (2.87 Å) of Zn488, and in return, the backbone carbonyl oxygen of Asp332 has the very long coordination distance of 2.38 Å.

In the X-ray structures of the enzyme—inhibitor complexes 1LAN<sup>8</sup> and 1LCP<sup>10</sup>, a hydrogen bond between the Zn488-bound oxygen of the tetrahedral group of the inhibitor and Lys262, which for its part is hydrogen-bonded to Asp332—O $\delta$ 1 and Asp332—O $\delta$ 2, was observed. Furthermore, the tetrahedral group interacts via two water molecules (or perhaps a carbonic acid molecule or a bicarbonate ion) with the positively charged guanidinium group of Arg336. In both structures, the inhibitor also interacts via water molecules with the backbone of the residues Leu360 and Gly362. A quantum chemical analysis<sup>12</sup> of the interactions of transition-state analogues with bLAP suggested that the strongest contribution to the inhibitor binding comes from the Zn<sup>2+</sup> ions followed by Lys262. The interaction of Leu360 is not significant. Overall, however, the available X-ray structures point to a variable coordination of the two Zn<sup>2+</sup> ions. This makes bLAP an ideal object for computational studies because the experimental results are compatible with many different coordination schemes. This coordinative flexibility also suggests that the nature of the coordination to the Zn<sup>2+</sup> ions may change significantly along the reaction path, a feature best revealed by calculations.

On the basis of the X-ray structures of the transition-state-analogue complexes and modeling studies with a L-leucine-L-valine substrate, several possible catalytic mechanisms have been proposed.<sup>8–10,13</sup> Two assumptions have been made: (a) because no covalent enzyme—inhibitor complexes have been found and

there are no active-site residues that could act as a nucleophile to attack the peptide carbonyl, a general base mechanism<sup>14</sup> has been suggested; (b) the reaction passes through a *gem*-diolate intermediate (Figure 3) that resembles the transition-state-analogue inhibitors.

The X-ray structures of the free enzyme (1LAM), the L-leucinal complex (1LAN), and the LeuP complex (1LCP) are thought to favor mechanism 1 (nomenclature as used in ref 10, see Figure 4). The nucleophile is coordinated as a bridging ligand, like the hydroxide ion in the free enzyme, and the coordination pattern of the tetrahedral intermediate corresponds to that observed in the LeuP and L-leucinal complexes. L-Leucinal that binds to bLAP in a hydrated form is assumed to be the most similar transition-state analogue to the natural substrate. The authors suggest that the substrate carbonyl oxygen is coordinated to Zn488 and a bridging hydroxide ion acts as the nucleophilic agent. The *gem*-diolate group of the resulting negatively charged tetrahedral intermediate is coordinated similarly to that of the inhibitor in the X-ray structures 1LCP and 1LAN. The protonated oxygen is a bridging ligand between the two metal ions and the second, unprotonated oxygen is additionally bound to Zn488. After the cleavage of the peptide bond, the peptide nitrogen is protonated by a water molecule. The function of Lys262 is to stabilize the substrate carbonyl carbon in the reactant structure and the unprotonated *gem*-diolate oxygen in the tetrahedral intermediate. Furthermore, there are stabilizing interactions to the guanidinium group of Arg336 and the backbone carbonyl oxygen of Leu360. This mechanism is shown in Figure 4. In mechanism 2 described in ref 10, the carbonyl carbon of the substrate is coordinated as a bridging ligand between the two Zn<sup>2+</sup> ions and the nucleophilic hydroxide is Zn488-bound. Mechanism 3 in ref 10 proposes Lys262 to be the acid for the protonation of the peptide nitrogen.

A further suggestion is based on the X-ray structure of aminopeptidase A (PepA) from *Escherichia coli*, which is isostructural to bLAP.<sup>13</sup> A bicarbonate ion bound to Arg356 (corresponding to Arg336 in bLAP) was found in the active site of this enzyme. The X-ray structure of native bLAP (1LAM) shows a bicarbonate in the same position, which is replaced by two water molecules in the enzyme—inhibitor complexes 1LAN and 1LCP. Moreover, the activity of PepA shows an 8-fold increase in the presence of bicarbonate ions in the buffer solution.<sup>13</sup> Because of bicarbonate contamination derived from dissolved carbon dioxide, even in degassed buffer solution, this effect may be stronger. Therefore, the bicarbonate ion has been proposed to act as a general base by deprotonating the bridging water molecule and protonating the peptide nitrogen. However, because of the relatively weak dependence of the activity of PepA on the bicarbonate concentration, this mechanism is not convincing. A much larger effect would be expected for an active role in the catalysis. More probable is an indirect contribution such as the regulation of the catalytic conditions. Additionally, mutagenesis experiments on Arg356 show only little contribution of this residue to the catalytic process. Thus, although a complete absence of bicarbonate in the buffer solution cannot be achieved, the R356A mutant is unable to bind any residual bicarbonate. A stronger contribution was found for Lys282 (corresponding to Lys262 in bLAP); the substitution of this residue by alanine lowers the activity by 2 orders of magnitude.

The structure of the active site suggests that a number of reaction paths are possible. Although some can be excluded by structural restrictions or general considerations, several must be calculated to be able to decide among the possibilities. At

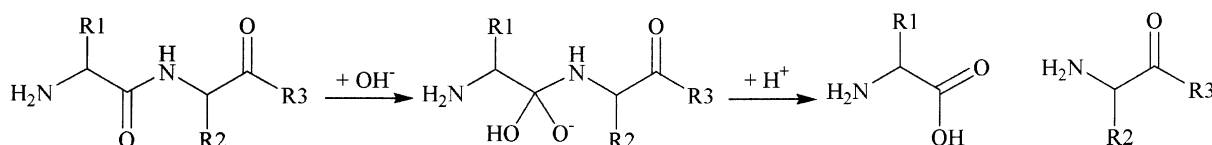


Figure 3. Schematic representation of the hydrolysis of a peptide bond passing a *gem*-diolate intermediate.

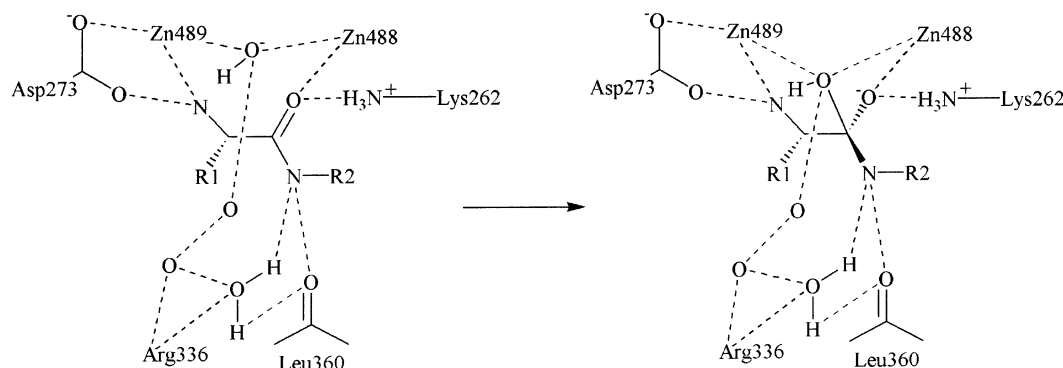


Figure 4. Possible catalytic mechanism for the hydrolysis of a peptide bond by bLAP proposed by Sträter and Lipscomb (mechanism 1 in ref 10).

best, a comparison among the results allows us to make a clear choice as to which path is the most favorable. This is the aim of this study.

Additionally, some specific questions concerning the structure of the active site and the function of the metal ions or the ligands are of interest. A crucial question is whether the nucleophile is coordinated to the  $\text{Zn}^{2+}$  ions as a bridging ligand as proposed in the literature.<sup>10</sup> Because the nucleophilicity of a 2-fold coordinated hydroxide ion is lower than that of a singly coordinated one, the possibility that the hydroxide is not bound to both metal ions in the enzyme–substrate complex must be considered. Another question is whether the carbonyl group of the peptide bond of the substrate is activated by coordination to one or both of the metal ions. Our earlier studies<sup>15–18</sup> on zinc hydrolases show a consistent pattern of the mode of action: the reaction is initiated by the deprotonation of a  $\text{Zn}^{2+}$ -bound water molecule that subsequently attacks the substrate. We have not yet found evidence for activation of the substrate by prior coordination to the  $\text{Zn}^{2+}$  ion.

## Method

A quantum mechanical description is essential for investigating the enzymatic reaction mechanism. High-level *ab initio* or DFT calculations give good results, but they require a very high computational effort for a model system that describes the active site sufficiently. Semiempirical calculations allow the treatment of a few hundred atoms, but they are also not suitable for systems of this size (with more than 8000 atoms in the monomer). We therefore chose a semiempirical quantum mechanical/molecular mechanical (QM/MM) approach with an active-site model including 176 atoms in the enzyme–substrate model. QM/MM techniques have been widely used<sup>19</sup> for the investigation of enzyme reaction mechanisms with considerable success and Gready and co-workers have carried out comprehensive systematic studies of the accuracy of various techniques.<sup>19a,c</sup>

Initial QM/MM studies with a rigid point charge environment, as we have used previously to investigate the mode of action of  $\text{PLA}_2$ <sup>20</sup> with good results, suggested that not only the electrostatic effects but also the mechanical response of the enzyme bulk to geometrical changes in the active site are important in the case of bLAP. The structure of transition-

state-analogue complexes is assumed to be similar to the structure of the tetrahedral intermediate of the substrate–enzyme complex. Especially, the shape of the binding pocket is not optimal for the reactants, products, or possible additional intermediates of the catalytic reaction. Furthermore, crystallization effects that are insignificant for a solvated enzyme influence the X-ray geometry. In the case of bLAP, geometry optimizations of some minima along the reaction path within a rigid lattice resulted in distorted active-site geometries. We therefore used a flexible enzyme environment that can respond to the reaction. This effect is consistent with the flexible nature of the coordination to the  $\text{Zn}^{2+}$  ions in the active site. Details of the QM/MM method are given in Appendix A. Note that, because of the large quantum mechanical system used, both the electrostatic and classical effects of the classical region are relatively small in this case (see below), so we have only validated the AM1 technique by comparison with density functional calculations.

**Computational Details.** All calculations were performed with the semiempirical program package VAMP 7.5.<sup>21</sup> We chose an alternating optimization strategy for the QM and MM parts, thus allowing the MM part to relax to the changes in the QM part and avoiding too many time-consuming QM calculations. For the QM optimization, we used the eigenvector following method<sup>22</sup> and for the MM optimization a low-memory Broyden–Fletcher–Goldfarb–Shannon (BFGS) algorithm.<sup>23</sup>

The point charges of the MM environment were generated by the Gasteiger–Marsili method<sup>24</sup> using Sybyl 6.6.<sup>25</sup> However, these were adjusted to yield an integer total charge if MM atoms were deleted during the model system generation.

No cutoff values were used for the calculation of van der Waals and Coulomb energies because this can cause energy discontinuities during geometry optimizations. Although this problem may be addressed by inclusion of switching functions, we chose the computationally more reliable alternative.

The Tripos force field<sup>26</sup> implemented in VAMP 7.5 was used for the MM part. Analogous parameters were created to substitute missing ones according to the original algorithm. Missing metal parameters were taken from the Sybyl program.<sup>25</sup> These parameters have not been validated but are adequate for structural metal ions, whereas the catalytic  $\text{Zn}^{2+}$  ions located in the active site are treated quantum mechanically.



The QM part contains the substrate model, the metal ions, and the active-site residues. The AM1 Hamiltonian<sup>27</sup> was used with the zinc parameters of Dewar and Merz.<sup>28</sup> A validation of the zinc parameters is given in Appendix B. All structures were optimized to a gradient norm of  $0.4 \text{ kcal mol}^{-1} \text{ \AA}^{-1}$ , and the stationary points were characterized by calculating the normal vibrations.

The use of a QM/MM approach with a flexible environment allows us to estimate the changes of the total energy of the enzyme. To ensure that there were no large initial gradients, the environment was relaxed with the tetrahedral intermediate substrate in the QM part. The relaxed environment was then used as a starting geometry for all further calculations.

The energies given are the total energies that include the energies of the two subsystems, the Coulomb-interaction energy, and the van der Waals-interaction energy. Energy deviations in the MM part can be interpreted as the response of the enzyme to the catalytic reaction in the active site.

Although semiempirical MO techniques are not generally regarded as state-of-the-art for the investigation of chemical reaction mechanisms, they are nonetheless still the best way to treat a model system that is large enough to allow the study of important geometrical changes within the coordination sphere of the metal-containing active site of an enzyme. Their speed allows far more comprehensive investigations of alternative reaction paths and the use of a large quantum mechanical system that moves the QM/MM boundary away from the active site. Nevertheless, the possible inaccuracies of the semiempirical methods should be kept in mind. In a study of the hydrolysis mechanism of formamide with various theoretical methods, Antonczak et al. showed that AM1 overestimates the activation energies but gives qualitatively similar results to higher-level methods.<sup>29</sup> However, our study is not intended to predict exact energies but rather to investigate the probability of different reaction paths by comparing the semiempirical energies. In this way, systematic errors cancel to a high degree, although the accuracy of the calculated activation barriers certainly is not adequate.

**System Partitioning.** Some constraints must be taken into account for the preparation of the starting structure. Both the QM and the MM part must be closed systems, so the total system must be divided and the fragments saturated with hydrogen atoms. The two subsystems were separated by cutting the backbone within the neighboring residues of amino acids included in the QM system. The cut was made between the  $C_\alpha$  atom and the peptide nitrogen at the N-terminus of the fragment or the carbonyl carbon at the C-terminus, leaving the peptide bonds in the QM part. The bonds to  $H_\alpha$  and  $C_\beta$  were also cut. The  $C_\alpha$  atoms were substituted by hydrogen atoms (see Figure 5). In this way, only weakly charged atoms are located at the direct borders between the QM and MM parts. The resulting amino acid fragments in the MM part were saturated by connecting the  $H_\alpha$  atom to the peptide nitrogen or carbonyl carbon of the backbone end. Remaining side chains that are no longer connected to the protein backbone were saturated using an additional hydrogen. The electrostatic and van der Waals interactions to the surrounding protein, together with weak harmonic constraints (with force constants of  $10\text{--}20 \text{ kcal mol}^{-1} \text{ \AA}^{-2}$ ) on the peptide C and N atoms of the backbone atoms in the QM part, ensure that the resulting QM model system retains its position. A validation of this procedure is described in ref 20. Additionally, to avoid artificial repulsive interactions between MM and QM parts causing large forces, the radii of the added hydrogens were reduced to  $0.1 \text{ \AA}$ .

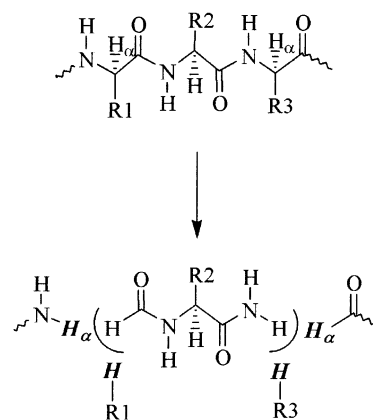


**Figure 5.** Schematic representation of the separation of a peptide chain into QM and MM parts. Here, the residue with the side chain R2 is supposed to be the QM region. The radii of the  $H_\alpha$  atoms and the hydrogens added to the residues R1 and R3 are reduced to  $0.1 \text{ \AA}$  to avoid artificial repulsion.

The protonation states of all acidic and basic residues were checked to describe the protein environment as well as possible. The total charge of the MM part should ideally be zero to avoid large forces on charged active sites. Therefore, some glutamate or aspartate residues positioned at the surface of the binding domain were protonated. This approximation is acceptable because the active site is located in the catalytic domain far away from the binding domain and, as outlined below, the surface of the protein would normally be complexed to other monomer units in the hexamer.

The free enzyme and the complex with LeuP were optimized to check the suitability of the semiempirical description of the active-site geometry and of the system-partitioning approach for the investigation of bILAP. The results are given in Appendix C. These systems were also used to study the influence of a carbonic acid molecule or bicarbonate ion (cf. Introduction) located near the active site.

**The Model System.** The QM part contains the metal ions (Zn488 and Zn489), their coordination ligands (Lys250, Asp255, Asp273, Asp332, and Glu334), a substrate model (Leu-Val), and Lys262. Furthermore, Ala333 was included in the QM part to obtain a continuous backbone fragment (Asp332-Ala333-Glu334) that stabilizes the geometry of the active site. With this exception, the model system corresponds to the active site shown in Figure 1. The MM part includes a carbonic acid molecule (CA environment, cf. Appendix C). Calculations were also performed with a bicarbonate ion (BIC) and without carbonic acid or bicarbonate (NOCA) in the environment. With some exceptions, the results are qualitatively equivalent both for the geometries and for the energies. All calculations are based on the X-ray structure of bILAP complexed with L-leucine-phosphonic acid (PDB entry 1LCP).<sup>10</sup>

## Results

The peptide bond to be cleaved has enantiotopic faces, and thus, two enantiomers of the tetrahedral intermediate resulting from nucleophilic attack on either the *re* or *si* faces of the carbonyl group are possible (see Figure 6). Assuming that the nucleophilic attack occurs from the metal center, the substrate in the reactant structure must adopt different conformations to form the two enantiomers because it is coordinated to Zn489 via its N-terminus. However, a rotation of the  $C_\alpha\text{--}C_{\text{carbonyl}}$  bond of the N-terminal leucine allows a transformation of one conformer to the other, especially because only the first and

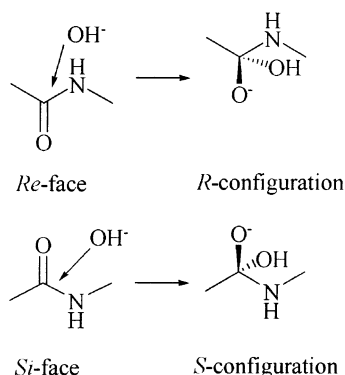


**Figure 6.** Enantiotopic faces and resulting enantiomers of the tetrahedral intermediate.

second N-terminal residues show significant interactions with the binding pocket of the enzyme.<sup>9</sup> Both possibilities have been investigated. In the following, the model describing the attack on the *re* face to give the *R* configuration of the tetrahedral intermediate is denoted **system R** and that for the *si* face and *S* configuration **system S**.

For clearness, the reaction path has been divided into partial steps. Each will be described in detail for both conformers of the substrate model. The first step is the deprotonation of a water molecule, followed by the nucleophilic attack, and finally the decomposition of the tetrahedral intermediate. If not denoted otherwise, the energies are given relative to the energy of the substrate–water complex of **system S**, which is the more stable.

**Structures and Reaction Path of the Enzyme–Substrate Complex. Deprotonation of the Nucleophilic Water Molecule.** In the water–substrate complex,  $E_{H_2O}$ , the water molecule is coordinated to Zn488. It is perfectly positioned to interact with the unprotonated Lys262. The hydrogen-bond pattern is very similar to that described for the LeuP complexes (cf. Appendix C), except that Lys262 is too far away from Asp255–O $\delta$ 2 for any interaction. Asp255 is coordinated to both Zn $^{2+}$  ions with O $\delta$ 2 forming a bridging ligand and O $\delta$ 1 additionally coordinated to Zn488. Additional hydrogen bonds occur between the N-terminus of the substrate and the water molecule and, in **system R**, between the water molecule and the substrate carbonyl carbon. In both systems, Asp332–O<sub>backbone</sub> is not coordinated to Zn488 but interacts with the water molecule. The water–substrate complex of **system S**,  $E_{H_2O}^S$  (the superscripts denote **system R** or **S**) is 12.7 kcal mol $^{-1}$  more stable than  $E_{H_2O}^R$ .

The activation barrier for the reaction  $E_{H_2O} \rightarrow E$  for **system S** is considerably higher than that for **system R** (the relative energies of the reaction paths are given in Table 1). This is also true for the relative energies of the resulting hydroxide–substrate complex, **E**. In **E**<sup>R</sup>, the substrate carbonyl carbon now interacts with Lys262, whereas in **E**<sup>S</sup>, a hydrogen-bond occurs between the peptide nitrogen of the substrate and the hydroxide ion, which is accompanied by a distortion of the peptide plane by 18.7°. In both systems, the hydroxide is only coordinated to Zn488 and forms a hydrogen bond to Lys262. The coordination patterns of Asp255 and Asp332–O<sub>backbone</sub> do not change significantly during this reaction step. The substrate carbonyl oxygen is not coordinated to one of the Zn $^{2+}$  ions in any of the structures involved. The geometries for **system R** are shown in Figure 7.

Sträter et al. proposed that the nucleophilic water might be deprotonated by a bicarbonate ion near the active site.<sup>13</sup> Our calculations including a bicarbonate, Gly335, and Arg336 in

**TABLE 1: Overview of Relative Energies (referring to  $E_{H_2O}^S$ ) in kcal mol $^{-1}$  of Intermediates and Transition States of the Reaction Steps in the Systems R and S within the CA Environment**

	system R		system S	
	relative energy	activation barrier	relative energy	activation barrier
$E_{H_2O}$	12.7		0.00	
$E_{H_2O} \rightarrow E$	25.2	12.5	21.7	21.7
<b>E</b>	22.0		19.3	
$E \rightarrow E_{\text{bridge}}$	24.6	2.6	25.5	6.2
$E_{\text{bridge}} \rightarrow E$	24.6	14.0	25.5	11.9
$E_{\text{bridge}}$	10.6		13.6	
$E \rightarrow \text{TI}$	34.5	12.5	38.9	19.6
$E_{\text{bridge}} \rightarrow \text{TI}$	36.9	26.3		
<b>TI</b>	24.8		22.5	
$\text{TI} \rightarrow \text{TI}_{\pm}$	45.3	20.5		
$\text{TI}_{\pm}$	42.5			
$\text{TI}_{\pm} \rightarrow \text{P}$	42.7	0.2		
$\text{TI} \rightarrow \text{diol}$	27.6	2.8	35.9	13.4
$\text{diol} \rightarrow \text{TI}$	27.6	14.1	35.9	16.4
<b>diol</b>	13.5		19.5	
$\text{diol} \rightarrow \text{P}$	64.0	50.5	75.9	56.4
$\text{TI} \rightarrow \text{P}_{\text{Leu}}^-$			72.1	49.6
$\text{P}_{\text{Leu}}^-$			0.0	
$\text{P}_{\text{Leu}}^- \rightarrow \text{P}$			1.3	1.3
<b>P</b>	−3.7		−19.1	

the QM part show that the activation energy for this proton transfer amounts to 36.4 kcal mol $^{-1}$  and, thus, is much less favorable than the deprotonation by Lys262.

**Formation of the Tetrahedral Intermediate.** A hydroxide ion must be present for the formation of the tetrahedral intermediate by a nucleophilic attack. A water molecule as the nucleophilic agent can be excluded because the nucleophilicity of neutral water is too low, especially when it is coordinated to one of the Zn $^{2+}$  ions.<sup>30</sup> Thus, the starting structure for the nucleophilic attack is the hydroxide–substrate complex, **E**.

Structure **E** can react in two ways: the hydroxide can attack the substrate carbonyl carbon to form the tetrahedral intermediate, **TI** (Figure 8, reaction path I), or it can occupy the bridging position between the two Zn $^{2+}$  ions to give the structure  $E_{\text{bridge}}$  (Figure 8, reaction path II). The activation barrier for the second possibility is considerably lower for both **systems R** and **S**. We were able to locate a transition state for the reaction  $E_{\text{bridge}}^R \rightarrow \text{TI}^R$  in **system R**, but it lies 13.8 kcal mol $^{-1}$  higher in energy than that for the nucleophilic attack of a Zn488-coordinated hydroxide. However, the barrier for the reformation of the hydroxide structure  $E_{\text{bridge}}^R \rightarrow E^R$  is 14.0 kcal mol $^{-1}$  and for  $E_{\text{bridge}}^S \rightarrow E^S$  11.9 kcal mol $^{-1}$ , so the Zn489–hydroxide coordination can be broken during the reaction and any equilibrium between bridged and monodentate hydroxide coordination must be considered to be dynamic.

In  $E_{\text{bridge}}^{R,S}$ , Asp332–O<sub>backbone</sub> is still not coordinated to Zn488. Asp255 is coordinated bidentately to Zn488; the coordination of Asp255–O $\delta$ 2 to Zn489 is broken. The transition state for the reaction step  $E_{\text{bridge}}^R \rightarrow \text{TI}^R$  shows a weak interaction between Zn488 and Asp332–O<sub>backbone</sub>, and Asp255 is now coordinated only via O $\delta$ 2 to Zn488. The hydroxide still occupies the bridging position, although the distance to Zn489 is longer than that to Zn488. The substrate carbonyl oxygen is also coordinated to Zn488, raising its coordination number to 6. However, Asp332–O<sub>backbone</sub> (coordination length 2.42 Å) and the substrate carbonyl carbon (coordination length 2.44 Å) are rather weak ligands. This structure is very similar to the geometry of LeuP3 (cf. Appendix C). This reaction step is shown in Figure 9.

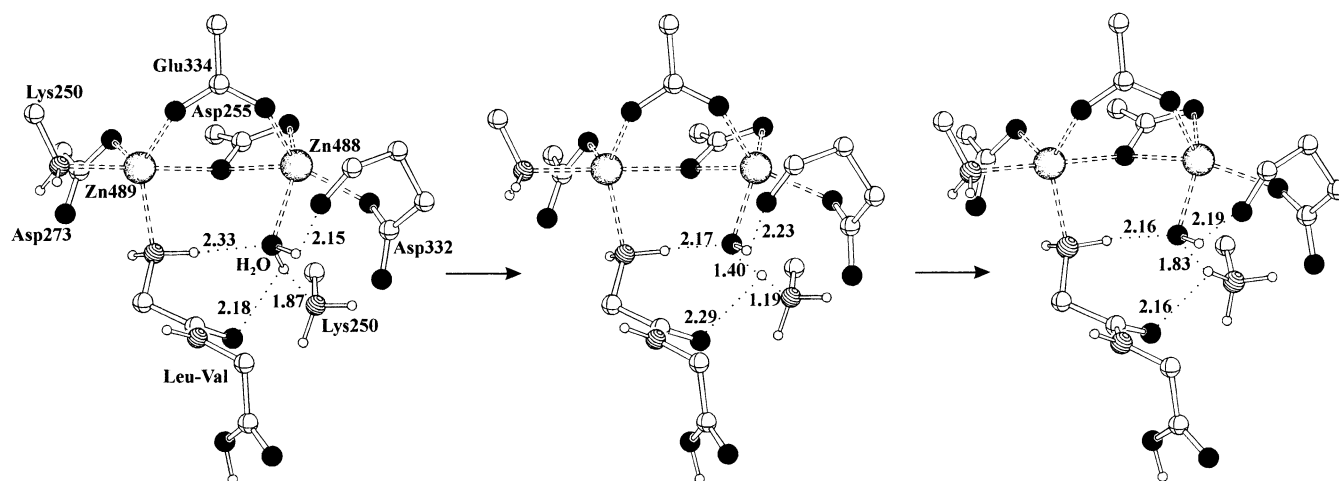


**Figure 7.** Deprotonation of the nucleophilic water  $E_{H_2O}^R \rightarrow E^R$  (for clarity, this figure, like the following representations of the active-site geometries, shows only a section of the QM part).

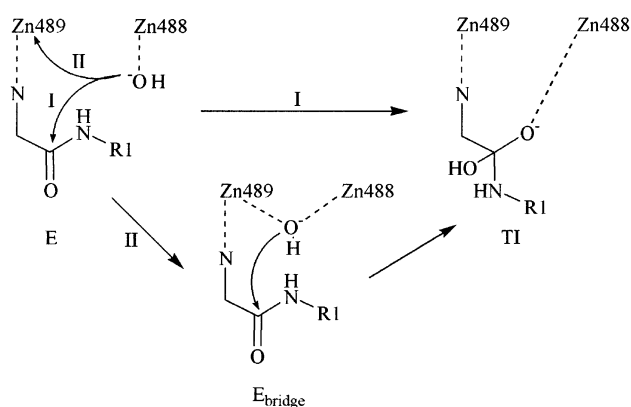


**Figure 8.** Formation of the tetrahedral intermediate—schematic representation of the reaction possibilities: path I,  $E^R \rightarrow TI^R$ ; path II,  $E^R \rightarrow E_{bridge}^R \rightarrow TI^R$ . Reaction path I is equivalent in **system S**; path II is only possible for **system R**; in **system S** no transition state for the nucleophilic attack from a bridging hydroxide could be found.

In the transition-state structure for the reaction step  $E^{R,S} \rightarrow TI^{R,S}$ , Asp332 and Asp255 are coordinated similarly as in that for  $E^R \rightarrow TI^R$ . Also, the carbonyl oxygen begins to interact with Zn488. Without a bridging hydroxide and without the Asp255–O $\delta$ 2 coordination, Zn489 actually has a coordination number of 4. As a result, Asp273–O $\delta$ 1 interacts with the metal ion, although as a weak ligand, especially in **system S**.

In the tetrahedral-intermediate structures,  $TI^{R,S}$ , the unprotonated *gem*-diolate oxygen, the former carbonyl oxygen, is now coordinated to Zn488. In **system R**, Lys262 forms a hydrogen bond to the unprotonated, in **system S** to the protonated, *gem*-diolate oxygen. Furthermore,  $TI^R$  has a hydrogen bond between the N-terminus and the unprotonated oxygen. Apart from these differences, the geometry of the active site is similar to those of the transition states  $E^{R,S} \rightarrow TI^{R,S}$ . The transition state and tetrahedral intermediate for **system R** are shown in Figure 10.

**Decomposition of the Tetrahedral Intermediate.** The peptide bond of the substrate must be broken and the peptide nitrogen protonated to form the product complex. Again, the system has several possible modes of reaction (see Figure 11). One possible proton donor is Lys262, which is positioned close to the *gem*-diolate group of the tetrahedral intermediate. It can transfer a proton either to the unprotonated *gem*-diolate oxygen, forming a neutral *gem*-diol, or to the peptide nitrogen, which results in a zwitterion. However, this proton transfer is only possible for

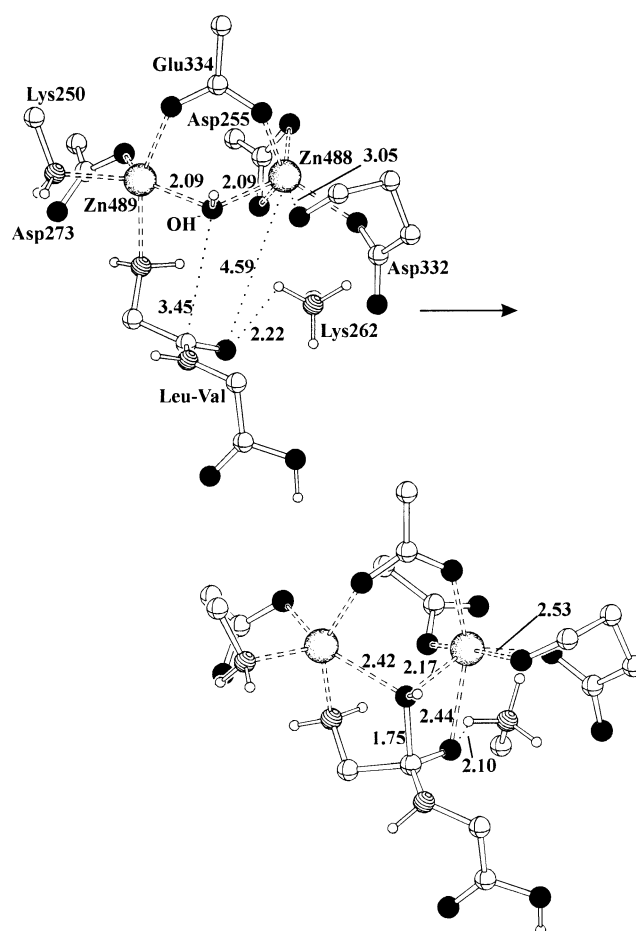


**Figure 9.** Formation of the tetrahedral intermediate: educt and transition-state structure for the reaction step  $E^R \rightarrow TI^R$ .

**system R**, because in **system S** the *gem*-diolate hydroxyl group is positioned directly between Lys262–N $\zeta$  and the peptide nitrogen. Another possible reaction path is a proton transfer from the *gem*-diolate group to the peptide nitrogen accompanied by the peptide-bond cleavage. This results in a negatively charged leucine fragment that can be reprotonated to facilitate the product release.

The reaction  $TI^R \rightarrow diol^R$  has a very low activation barrier. The Asp332–O<sub>backbone</sub> coordination to Zn488 is weakened to favor a hydrogen bridge to the *gem*-diolate hydroxyl group. The



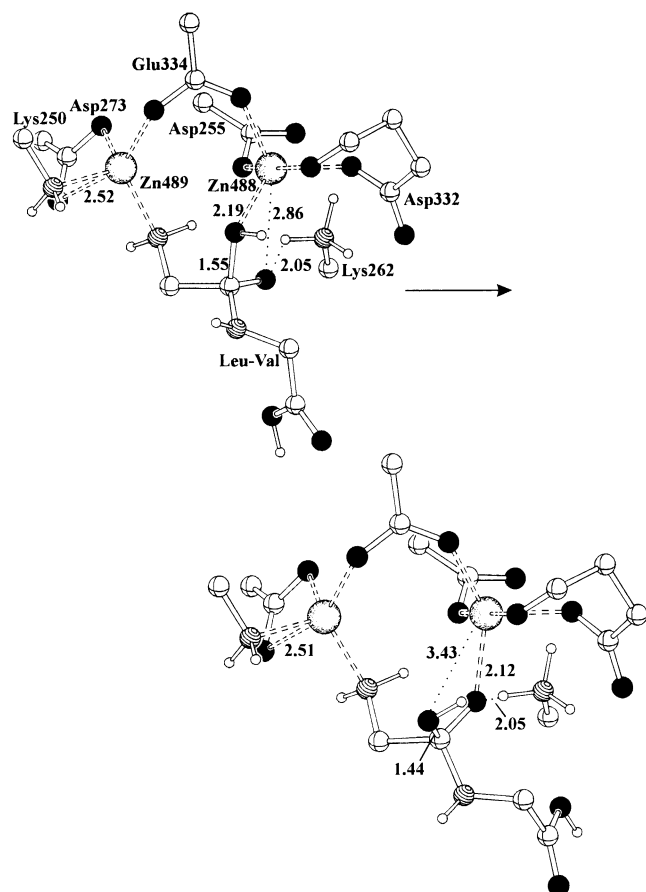


**Figure 10.** Formation of the tetrahedral intermediate: transition state and product structure for the reaction step  $E^R \rightarrow TI^R$ .

*gem*-diolate is no longer bound to Zn488, but Asp255 becomes a bidentate ligand. In the resulting structure,  $diol^R$ , Asp255–Oδ2 is also coordinated to Zn489, which in return has lost its interaction to Asp273–Oδ1. The *gem*-diol hydroxyl group formed by the proton transfer has the *E* conformation. Figure 12 shows the geometries of the transition state and the diol structure of **system R**.

The reaction  $TI^S \rightarrow diol^S$  formally results in the same structure as that for **system R**, but in **system S**, the *gem*-diol group has the *Z* conformation and there are differences in the conformation of the substrate, especially of the valine fragment. The Asp255 coordination is that of **system R**. The different orientation of the valine side chain makes the calculation of the obvious reaction possibility  $diol^S \rightarrow TI^R$  difficult, because the unprotonated *gem*-diolate oxygen cannot be coordinated to Zn488. However, in this study, dynamic effects are not taken into account. The reaction  $diol^S \rightarrow diol^R$ , which means a rotation of the diol-hydroxyl group and of the valine side chain, should occur during the normal protein movements. In this way, there is a possibility of a racemizing reaction.

The further reaction of the *gem*-diol is a proton transfer from a hydroxyl group to the peptide nitrogen. However, the activation barrier of this reaction was found to be more than 50 kcal mol<sup>-1</sup> in both **systems R** and **S** and, thus, clearly is very unfavorable. The addition of a water molecule that may act as a proton shuttle between the *gem*-diol and the peptide nitrogen is possible, but the activation energy is not significantly lower.

The other possible proton transfer in **system R** with Lys262 as the proton donor is the transfer to the peptide nitrogen. Indeed, this reaction step,  $TI^R \rightarrow TI_{\pm}^R$  is much more favorable with an activation energy of 20.5 kcal mol<sup>-1</sup>. In the transition-state

structure, Asp255 changes its coordination pattern again, because the Zn488–Asp255–Oδ1 coordination is broken, while Oδ2 still acts as a bridging ligand. This pattern is conserved in the zwitterionic structure  $TI_{\pm}^R$ . This structure is a very shallow minimum, and the product complex can be formed virtually without activation energy.

In the product complex,  $P^R$ , the valine fragment of the substrate hardly shows any interactions with the active-site residues at all. The leucine fragment is only bound to Zn489. Both products should be released easily, especially if the N-terminus of the leucine is protonated. Figure 13 shows the reaction  $TI^R \rightarrow TI_{\pm}^R \rightarrow P^R$ .

In **system S**, the formation of a zwitterion by the proton transfer from Lys262 to the peptide nitrogen is not possible (see Figure 14). Instead, a concerted transfer from the *gem*-diolate group to the nitrogen and peptide-bond cleavage was found as a possible reaction. However, similarly to the reaction  $diol \rightarrow P$ , this step has a very high activation energy (49.6 kcal mol<sup>-1</sup>). This reaction step is shown in Figure 14. The product  $P_{Leu}^S$  has a negatively charged leucine fragment that is still coordinated to Zn488. This can easily be protonated by Lys262 to form the product,  $P^S$ . While the Asp255 coordination in the transition state of the reaction  $TI^S \rightarrow P_{Leu}^S$  and the structure  $P_{Leu}^S$  is like that in  $TI^S$ ,  $P^S$  shows the same pattern as  $P^R$ .

Sträter and Lipscomb suggested that the proton donor for the decomposition step is an additional water molecule.<sup>10</sup> This is possible in **system R** because the hydroxide ion formed by the proton transfer from the water to the peptide nitrogen in return abstracts a proton from Lys262 and so acts as a proton shuttle. However, the activation barrier amounts to 36.0 kcal mol<sup>-1</sup>, and this reaction is clearly less favorable than a direct proton transfer from Lys262 to the peptide nitrogen. No minimum for this reaction could be found in **system S** because the water cannot approach the peptide nitrogen in a way that allows the resulting hydroxide to be stabilized.

The most favorable reaction path for the decomposition of the tetrahedral intermediate is that via the zwitterionic structure in **system R**. The rate-limiting step, also for the whole reaction, is the proton transfer from Lys262 to the peptide nitrogen.

**Substrate Binding and Product Release.** Although the QM/MM calculations do not take entropic effects, which often contribute strongly to the substrate binding process, into account, some considerations are of interest. The N-termini of peptides are usually positively charged at physiological pH. They must be deprotonated to coordinate to the Zn<sup>2+</sup> ion. This may happen outside the active site, but one possible candidate for the proton acceptor is the bridging hydroxide ion found in the free enzyme structure 1LAM.<sup>8</sup> The protonated N-terminus of the substrate can transfer a proton to the hydroxide with an activation barrier of 16.4 kcal mol<sup>-1</sup>. In the presence of the substrate, the resulting water molecule breaks its coordination to Zn489 and remains only bound to Zn488. Subsequently, the N-terminus can be coordinated to Zn489 with an activation energy of 6.4 kcal mol<sup>-1</sup>. The resulting structure is that of the water–substrate complex,  $E_{H_2O}$ . The starting structure, with a bridging hydroxide and a protonated N-terminus of the substrate, is 9.0 kcal mol<sup>-1</sup> higher in energy than this complex.

The release of the Zn489-coordinated leucine fragment can be facilitated by the protonation of the N-terminus by a water molecule. Coordination of an additional water molecule to either of the two Zn<sup>2+</sup> ions is possible. In both cases, the water is first coordinated and the Zn489–nitrogen coordination is subsequently broken before the proton transfer takes place. The resulting hydroxide ion can then occupy a bridging position.

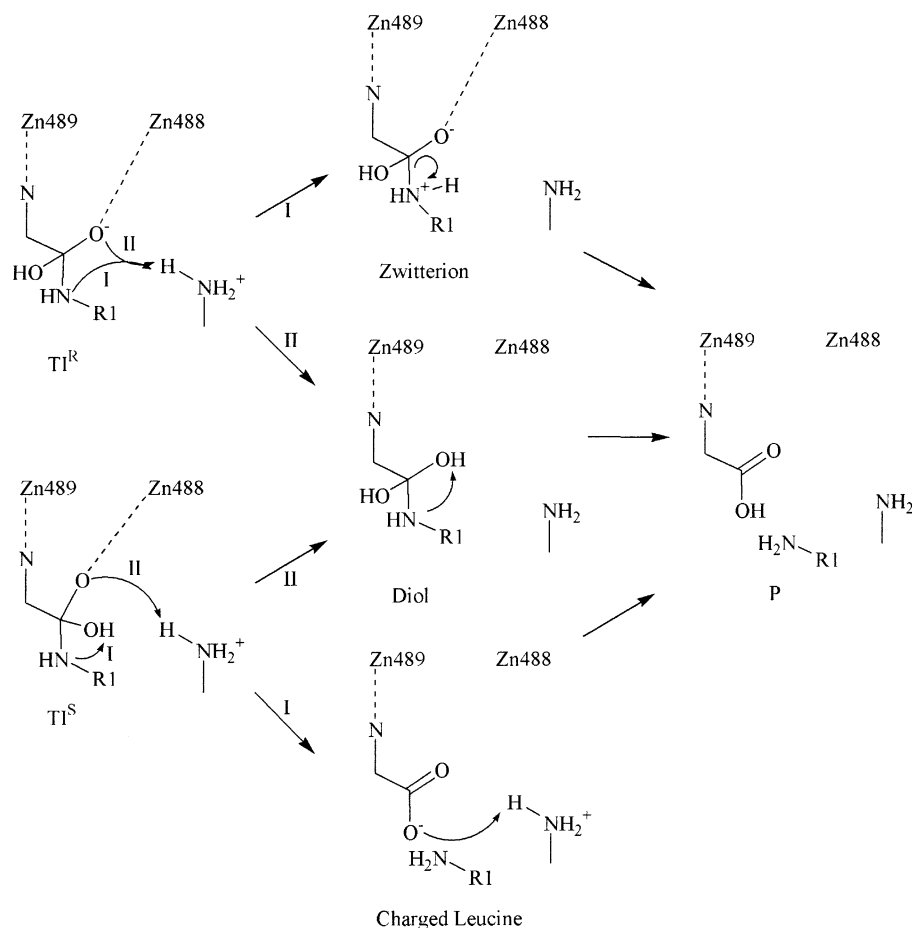


**Figure 11.** Decomposition of the tetrahedral intermediate: schematic representation of the reaction possibilities of  $\text{TI}^{\text{R}}$  (path I,  $\text{TI}^{\text{R}} \rightarrow \text{TI}^{\text{R}}_{\pm}$ ; path II,  $\text{TI}^{\text{R}} \rightarrow \text{diol}^{\text{R}}$ ) and  $\text{TI}^{\text{S}}$  (path I,  $\text{TI}^{\text{S}} \rightarrow \text{P}^{\text{S}}_{\text{Leu-}}$ ; path II,  $\text{TI}^{\text{S}} \rightarrow \text{diol}^{\text{S}}$ ). The structures of  $\text{diol}^{\text{R}}$  and  $\text{diol}^{\text{S}}$  are formally the same.

The rate-limiting step is the proton transfer with an activation energy of 20.3 kcal mol<sup>-1</sup> if the water is coordinated to Zn488 and 22.6 kcal mol<sup>-1</sup> for a Zn489-coordinated water. In the resulting structures, the N-terminus of the leucine fragment interacts via hydrogen bonds with the hydroxide ion and with Lys262. The energy varies strongly with the position and conformation of the substrate fragments; therefore, the final structures, although they formally have the same constitution, differ by 15.9 kcal mol<sup>-1</sup> in energy. In the final structures, a hydroxide ion occupies the bridging position and the N-terminus of the leucine is protonated. They are 7.7 kcal mol<sup>-1</sup> (if the water coordinates to Zn488) and 31.9 kcal mol<sup>-1</sup> (Zn489-coordinated water) higher in energy than the corresponding starting structures, which is a product complex with an uncoordinated water.

Another possible proton shuttle for the binding or release process is a bicarbonate ion or carbonic acid molecule near the active site. The activation barrier for the proton transfer from the protonated N-terminus of the substrate to the bicarbonate ion is 13.5 kcal mol<sup>-1</sup>, which is slightly lower than that for the proton transfer to a bridging hydroxide ion; the barrier from the carbonic acid to the coordinated leucine amino group in the product structure is 34.9 kcal mol<sup>-1</sup>. The energy differences between starting and product structures are 9.9 kcal mol<sup>-1</sup> for the binding process (the neutral N-terminus is not yet coordinated to Zn489) and 28.7 kcal mol<sup>-1</sup> for the release.

**Mechanical and Electrostatic Effects of the Enzyme Environment.** *Mechanical Effects.* The energy partitioning inherent in the QM/MM technique allows us to analyze different energy contributions to the reaction mechanism conveniently.

For instance, the mechanical response of the enzyme to the catalytic reaction is given by comparing the total energy profiles of the reaction profiles to those including only the QM and QM/MM interaction energies without the contribution of the MM part (Figure 15).

A striking difference between the systems is that the relative total energies of most transition states and intermediates in **system R** are lower than the pure QM energies, whereas in **system S** the situation is reversed. In **system R**, all activation barriers are smaller than their QM equivalents. The largest difference occurs in the reaction step  $\text{E}^{\text{R}} \rightarrow \text{TI}^{\text{R}}$ , where the QM/MM activation energy is 5.9 kcal mol<sup>-1</sup> lower than its QM counterpart. The situation is similar for  $\text{diol}^{\text{R}} \rightarrow \text{P}^{\text{R}}$ ,  $\text{TI}^{\text{R}} \rightarrow \text{diol}^{\text{R}}$  and, more importantly, for  $\text{diol}^{\text{R}} \rightarrow \text{TI}^{\text{R}}$ . The reaction  $\text{TI}^{\text{R}} \rightarrow \text{diol}^{\text{R}}$  is actually a dead-end because of the very high activation energy for the further reaction  $\text{diol}^{\text{R}} \rightarrow \text{P}^{\text{R}}$ . However, both the activation barrier for the competing reaction  $\text{TI}^{\text{R}} \rightarrow \text{TI}^{\text{R}}_{\pm}$  and that for the return reaction  $\text{diol}^{\text{R}} \rightarrow \text{TI}^{\text{R}}$  are significantly lower. Interestingly, for both dead-end structures,  $\text{diol}^{\text{R}}$  and  $\text{E}^{\text{R}}_{\text{bridge}}$ , the CA environment is the one that favors the return reaction best. When the BIC systems are used, the reaction  $\text{diol}^{\text{R}} \rightarrow \text{TI}^{\text{R}}$  requires an even higher activation energy than the rate-limiting step. This is reasonable because the bicarbonate destabilizes the negatively charged tetrahedral-intermediate structure, to which the transition state is similar.

*Electrostatic Effects.* In the classical picture of enzyme catalysis, both the mechanical effect of the enzyme environment and its electrostatic influence are suggested to favor the catalytic reaction. A dielectric constant of  $\epsilon = 4$  was assumed for the



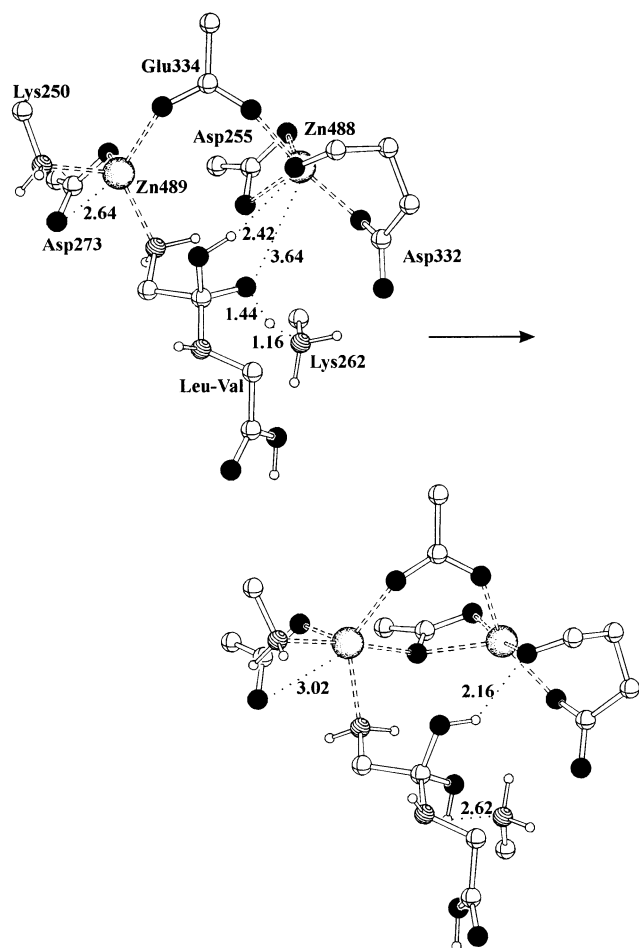


**Figure 12.** Transition state and product structure of the reaction step  $\text{TI}^{\text{R}} \rightarrow \text{diol}^{\text{R}}$ .

calculations. To investigate the effect of the electrostatic effect, single-point calculations using a dielectric constant of  $\epsilon = 1$  (the Coulomb interaction is switched on) and  $\epsilon = 10^6$  (the Coulomb interaction is completely switched off) on the stationary points of the reaction courses were performed. For these calculations, the environment was described merely by point charges without associated van der Waals potentials. In this way, the effect of the electrostatic influence on the reaction can be studied without any additional perturbation. Figure 16 shows the QM energy profiles for the **systems R** and **S** within the CA environment.

With the exception of the product structure,  $\text{P}^{\text{R}}$ , for which a higher relative energy might even have a positive effect on the turnover number of the protein, and the transition states for the reaction steps  $\text{E}_{\text{bridge}}^{\text{R}} \rightarrow \text{TI}^{\text{R}}$  and  $\text{diol}^{\text{R}} \rightarrow \text{P}^{\text{R}}$ , the relative energies of the intermediates and transition states of **system R** are lowered by the electrostatic influence. As a consequence, the activation energies for the unfavorable steps  $\text{E}_{\text{bridge}}^{\text{R}} \rightarrow \text{TI}^{\text{R}}$  and  $\text{diol}^{\text{R}} \rightarrow \text{P}^{\text{R}}$  are higher. Furthermore, the barriers for  $\text{E}^{\text{R}} \rightarrow \text{TI}^{\text{R}}$  and  $\text{E}^{\text{R}} \rightarrow \text{E}_{\text{bridge}}^{\text{R}}$  are also 4.0 and 4.4 kcal mol<sup>-1</sup>, respectively, higher because of the stronger stabilization of  $\text{E}^{\text{R}}$ . However, this has no influence on the favored reaction path, because the activation barrier for the nucleophilic attack is still lower than that of the rate-limiting step  $\text{TI}^{\text{R}} \rightarrow \text{TI}_{\pm}^{\text{R}}$ , which, in contrast, is slightly lowered. Moreover, the barrier for the step  $\text{E}_{\text{bridge}}^{\text{R}} \rightarrow \text{E}^{\text{R}}$ , which leads back to the more favorable path, is also lowered. Only the stronger stabilization of  $\text{diol}^{\text{R}}$  has a negative effect, because the activation energy for  $\text{diol}^{\text{R}} \rightarrow \text{TI}^{\text{R}}$

is 2.4 kcal mol<sup>-1</sup> higher, but still lower than that of the rate-limiting step.

In **system S**, all relative energies are lowered under the influence of the electrostatic effect. This also applies to the activation barriers for the reaction steps  $\text{E}_{\text{H}_2\text{O}}^{\text{S}} \rightarrow \text{E}^{\text{S}}$ ,  $\text{E}^{\text{S}} \rightarrow \text{TI}^{\text{S}}$ , and  $\text{P}_{\text{Leu}}^{\text{S}} \rightarrow \text{P}^{\text{S}}$ , whereas for the reaction steps  $\text{E}^{\text{S}} \rightarrow \text{E}_{\text{bridge}}^{\text{S}}$ ,  $\text{TI}^{\text{S}} \rightarrow \text{P}_{\text{Leu}}^{\text{S}}$ ,  $\text{TI}^{\text{S}} \rightarrow \text{diol}^{\text{S}}$ , and  $\text{diol}^{\text{S}} \rightarrow \text{P}^{\text{S}}$  the activation energies are higher. This effect shows clearly that the enzyme favors the **system R** reaction path via the zwitterionic intermediate  $\text{TI}_{\pm}^{\text{R}}$ .

## Discussion

Sträter and Lipscomb<sup>10</sup> based their suggestions for catalytic mechanisms on the 3D structure of the bLAP–LeuP complex. They assumed that the coordination pattern of the tetrahedral intermediate is similar to that in the enzyme–inhibitor complex. The X-ray structure shows one of the phosphonate oxygens as a bridging ligand and another bound to Zn488. However, the geometry optimization of the inhibitor structures (see Appendix C) showed that this coordination is only possible for a completely deprotonated phosphonate group with a charge of  $-2$ . The better transition-state analogue is probably an inhibitor with a charge of  $-1$ . For this system, the coordination pattern is different. This result is supported by the calculation of the tetrahedral-intermediate structure of the enzyme–substrate model system, although neither of the single-protonated inhibitor structures resembles the  $\text{Zn}^{2+}$  coordination of the *gem*-diolate group exactly. However, the P–O and P–C bonds of the phosphonate group are longer than the corresponding C–O and C–C bonds in the *gem*-diolate, which allows the inhibitor ligand to coordinate to Zn489 in addition to the N-terminus, and moreover, the inhibitor consists of only one residue. The valine side chain of the substrate model Leu–Val restricts its flexibility, which is also true for a natural substrate.

The peptide bond of the reactant structures coordinated via the N-terminus shows no interaction to either of the two metal ions. The substrate backbone must be twisted to achieve a coordination of the carbonyl carbon in both **systems R** and **S**. Because of the rigidity of the peptide group, this would lead to large conformational changes of the side chains. Sträter and Lipscomb's assumption that the nucleophilic agent is a bridging hydroxide ion is also based on the inhibitor coordination pattern observed in the X-ray structure. Although this kind of attack is possible for **system R**, it is not surprising that the nucleophilic attack by a Zn488-coordinated hydroxide is more favorable because the nucleophilicity of the doubly coordinated hydroxide must be lower. A water molecule has been suggested to be the acid that protonates the peptide nitrogen, but the strong dependence of the enzyme activity on Lys262<sup>13</sup> indicates that this residue is involved in the rate-limiting step. This is in agreement with the result of the calculations. Lys262 acts as the proton donor for the decomposition of the tetrahedral intermediate, which is the rate-limiting step of the most favorable reaction path.

A remarkable feature of the active site is the flexibility of the ligands Asp273, Asp332–O<sub>backbone</sub>, and, especially, Asp255, which is able to provide one additional ligand to each of the  $\text{Zn}^{2+}$  ions by coordinating the Zn488-bound Oδ2 additionally to Zn489 and by coordinating Oδ1 to Zn488, forming a bidentate ligand to this metal ion. The Asp255 coordination changes are partly accompanied, or caused, by changes in the coordination of Asp273 or Asp332. Asp255–Oδ1 is coordinated to Zn488 if either Asp332–O<sub>backbone</sub> is involved in hydrogen bonds and not bound to the metal ion (in  $\text{E}_{\text{H}_2\text{O}}^{\text{R,S}}$ ,  $\text{E}^{\text{R,S}}$  and  $\text{E}_{\text{bridge}}^{\text{R,S}}$ ).

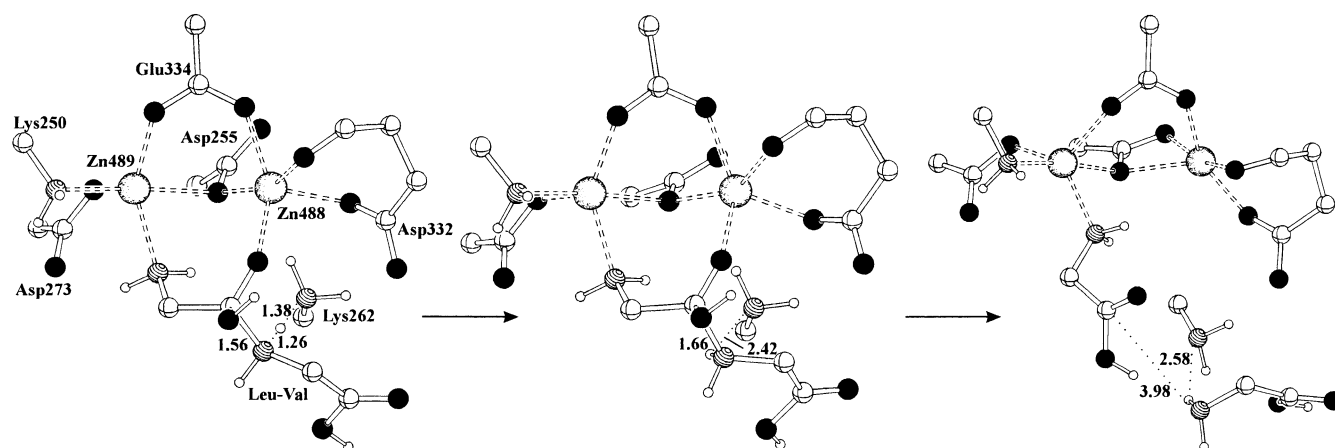


**Figure 13.** Decomposition of the tetrahedral intermediate: transition state and product structure of the reaction step  $\text{TI}^{\text{R}} \rightarrow \text{TI}_{\pm}^{\text{R}}$  and the product  $\text{P}^{\text{R}}$ .

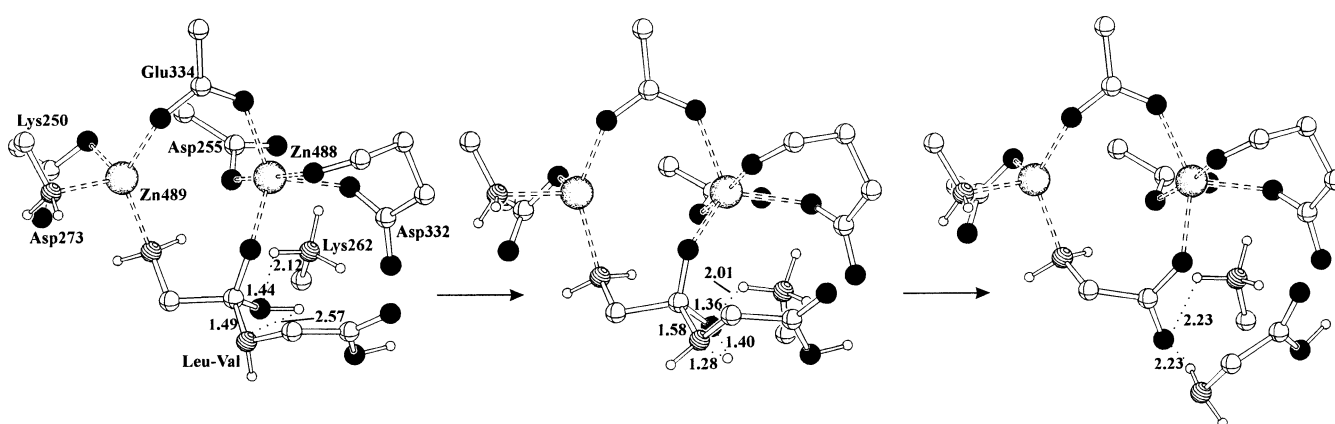


**Figure 14.** Decomposition of the tetrahedral intermediate: educt, transition-state, and product structure of the reaction step  $\text{TI}^{\text{S}} \rightarrow \text{P}_{\text{Leu-}}^{\text{S}}$ .

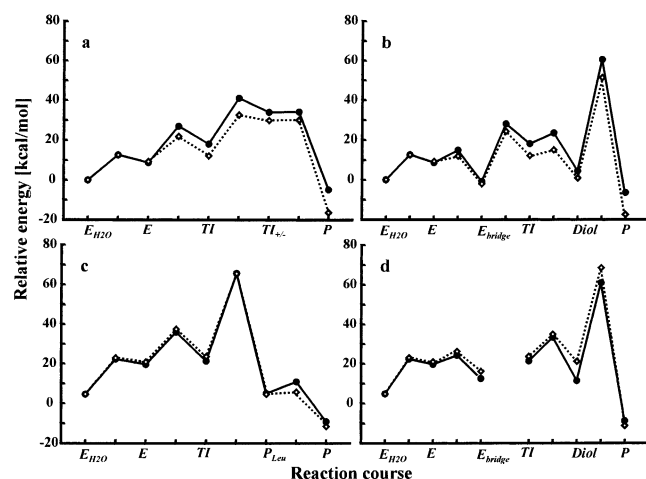


**Figure 15.** Energy profiles of (a) system  $\text{R } \text{E}_{\text{H}_2\text{O}}^{\text{R}} \rightarrow \text{E}^{\text{R}} \rightarrow \text{TI}^{\text{R}} \rightarrow \text{TI}_{\pm}^{\text{R}} \rightarrow \text{P}^{\text{R}}$ , (b) system  $\text{R } \text{E}_{\text{H}_2\text{O}}^{\text{R}} \rightarrow \text{E}^{\text{R}} \rightarrow \text{E}_{\text{bridge}}^{\text{R}} \rightarrow \text{TI}^{\text{R}} \rightarrow \text{diol}^{\text{R}} \rightarrow \text{P}^{\text{R}}$ , (c) system  $\text{S } \text{E}_{\text{H}_2\text{O}}^{\text{S}} \rightarrow \text{E}^{\text{S}} \rightarrow \text{TI}^{\text{S}} \rightarrow \text{P}_{\text{Leu-}}^{\text{S}} \rightarrow \text{P}^{\text{S}}$ , and (d) system  $\text{S } \text{E}_{\text{H}_2\text{O}}^{\text{S}} \rightarrow \text{E}^{\text{S}} \rightarrow \text{E}_{\text{bridge}}^{\text{S}} \rightarrow \text{TI}^{\text{S}} \rightarrow \text{P}^{\text{S}}$ . Circles and solid lines denote the QM energy including the van der Waals- and Coulomb-interaction energy with the MM part; diamonds and dotted lines denote the total QM/MM energy of the system. The structures  $\text{E}_{\text{H}_2\text{O}}^{\text{R}}$ ,  $\text{E}^{\text{R}}$ ,  $\text{TI}^{\text{R}}$ , and  $\text{P}^{\text{R}}$  within system  $\text{R}$  (parts a and b) and system  $\text{S}$  (parts c and d) are identical so that a combination of reaction paths is possible.

or the binding site initially occupied by the water molecule is vacant (in  $\text{diol}^{\text{R,S}}$  and  $\text{P}^{\text{R,S}}$ ). With the one exception of the transition state  $\text{E}_{\text{bridge}}^{\text{R}} \rightarrow \text{TI}^{\text{R}}$ , the Zn488 coordination number

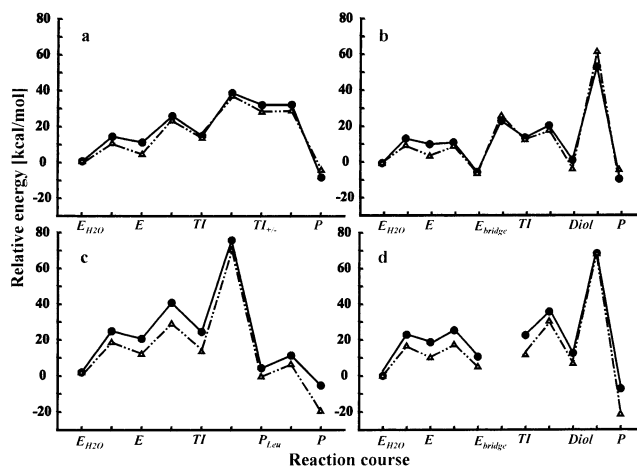


**Figure 16.** Energy profiles of the different reaction paths (cf. Figure 15) calculated with a dielectric constant  $\epsilon = 10^6$  (circles/solid lines; Coulomb interaction switched off) and  $\epsilon = 1$  (triangles/stroked lines; Coulomb interaction switched on). The protein environment for this calculation is described by point charges without associated van der Waals potentials.

is always 5. Zn489–Asp255–Oδ2 coordination does not occur if an additional binding site is occupied (in  $\text{E}_{\text{bridge}}^{\text{R,S}}$ ) or if the substrate coordinated to Zn489 via its N-terminus has a negative charge (in  $\text{TI}^{\text{R,S}}$  and  $\text{P}_{\text{Leu-}}^{\text{S}}$ ). In this case, the fifth binding site is, at least partially, occupied by Asp273–Oδ1 and it does not seem to be necessary for Zn489 to interact with Asp255–Oδ2.

In  $\text{TI}^{\text{S}}$  and  $\text{P}_{\text{Leu}^-}^{\text{S}}$ , the coordination number can be considered to be 4 if the  $\text{Zn489-Asp273-O}\delta 1$  interaction is neglected. However, the  $\text{Zn489-Asp273-O}\delta 1$  distances are 2.84 Å in  $\text{TI}^{\text{S}}$  and 2.72 Å in  $\text{P}_{\text{Leu}^-}^{\text{S}}$ , not much longer than the  $\text{Zn488-Asp332-O}_{\text{backbone}}$  distances in some structures (the largest distance is 2.66 Å in  $\text{diol}^{\text{R}}$ , in which  $\text{Asp332-O}_{\text{backbone}}$  is additionally involved in a hydrogen bond to the *gem*-diol group). In this respect, the assignment of coordination numbers to the  $\text{Zn}^{2+}$  ions is arbitrary. The changes in the ligand coordination accompany the geometry changes during the reaction path automatically. The simulation of a reaction step leads to reproducible coordination patterns, regardless of whether the starting structure is the reactant or the product of this step. This effect is not reproduced by a smaller pure QM system. Obviously, a large active-site model and the flexibility of the side chains are necessary to reproduce this response to the catalytic reaction.

The  $\text{Zn}^{2+}$  ions have different functions. While the main role of Zn489 is to bind and hold the substrate via the N-terminus, Zn488 binds the nucleophilic water molecule and allows a proton transfer to Lys262 by lowering the  $\text{p}K_{\text{a}}$  value of the water<sup>30</sup> and providing a suitable topology. It also binds and stabilizes the resulting hydroxide ion, which is well-positioned for the nucleophilic attack, and the negatively charged tetrahedral intermediate that in turn is well-positioned for the proton transfer from Lys262 to the peptide nitrogen. As soon as the reaction has taken place, Zn488 has no interactions with either of the products. The changes in the Zn489 coordination pattern when it binds a negatively charged substrate indicate that it may also partially stabilize the structures  $\text{TI}^{\text{R,S}}$  and  $\text{P}_{\text{Leu}^-}^{\text{S}}$ , although Zn488 must make the main contribution, because it interacts directly with the charged *gem*-diolate group in  $\text{TI}^{\text{R,S}}$  or the carboxylate group in  $\text{P}_{\text{Leu}^-}^{\text{S}}$ .

Aside from the  $\text{C}_{\alpha}$  chirality of the substrate protein, which is untouched by the hydrolysis, neither the reactants nor the products are chiral. However, the reaction clearly prefers an enantioselective path.

The carbonic acid, a bicarbonate ion is obviously unfavorable because of the destabilizing effect on the negatively charged tetrahedral intermediate, is certainly not essential for the catalytic process. The only clear difference obtained with the CA environment to the BIC or NOCA environment is the stronger stabilization of the reaction  $\text{diol}^{\text{R}} \rightarrow \text{TI}^{\text{R}}$ . The activation barrier of  $\text{diol}^{\text{R}} \rightarrow \text{TI}^{\text{R}}$  in the BIC environment is 23.0 kcal mol<sup>-1</sup> (2.5 kcal mol<sup>-1</sup> higher than that of the rate-limiting step), that in the NOCA environment is 18.7 kcal mol<sup>-1</sup> (1.8 kcal mol<sup>-1</sup> lower than the rate-limiting step), whereas the CA environment clearly supports this step by lowering the barrier to 14.1 kcal mol<sup>-1</sup> (6.4 kcal mol<sup>-1</sup> lower than the rate-limiting step).

The QM/MM approach using a semiempirical QM technique allows us to use a large QM model system. This ability to describe the whole active site compensates for the possibly less-accurate semiempirical methods compared to ab initio or DFT techniques for effects such as the coordination changes during the course of the reaction. The activation barriers are probably too high, but nevertheless, the relationship between the barriers of the different reaction steps can be estimated. To assess possible errors introduced by AM1, we performed single-point PW91/DNP<sup>31,32</sup> calculations with DMol<sup>3,32</sup> implemented in the program package Materials Studio<sup>33</sup> on the most significant points along the reaction path and compared them with the unperturbed (gas-phase single points) AM1 results. Figure 17 shows a comparison of the two methods. Clearly, the transition state for the initial water deprotonation and the relative energy

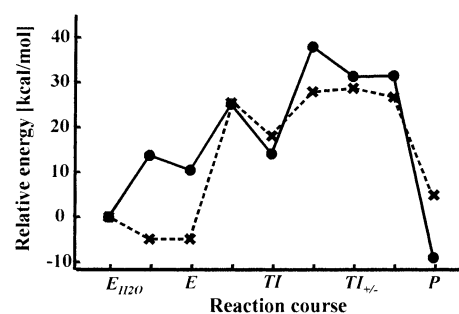


**Figure 17.** Comparison between the energy profile of the most favorable reaction path  $\text{E}_{\text{H}_2\text{O}}^{\text{R}} \rightarrow \text{E}^{\text{R}} \rightarrow \text{TI}^{\text{R}} \rightarrow \text{TI}_{\text{w}}^{\text{R}} \rightarrow \text{P}^{\text{R}}$  obtained by single-point calculations in the gas phase of the optimized structures with AM1 (circles/solid lines) and DMol<sup>3</sup> (PW91/DNP) (crosses/dashed lines).

of the initial hydroxide complex are too high with AM1. However, the relative energies of the remaining steps show remarkably good agreement between the two techniques. The shape of the DFT energy profile does suggest that the zwitterionic tetrahedral intermediate may be an artifact of the semiempirical calculations and that the final protonation/dissociation step may be concerted. In general, however, Figure 17 suggests that the AM1 results at least give a good qualitative picture of the reaction mechanism.

Unlike our earlier work on the mode of action of  $\text{PLA}_2$ ,<sup>20</sup> in which the influence of the enzyme environment is mainly electrostatic and, thus, a rigid point charge lattice could be used, the calculation on the bILAP system requires a flexible environment. In the current example, the semiempirical QM/MM-hybrid approach has demonstrated its ability to describe both the electrostatic and the mechanical effects of the enzyme environment on catalysis. Nevertheless, the current investigation reports only static results. In future work, consideration of the free energy profiles by QM/MM molecular dynamics simulations will become necessary.

**Acknowledgment.** The authors thank the Deutsche Forschungsgemeinschaft and the Stiftung Volkswagenwerk for financial support.

## Appendix A

**QM/MM Method.** Our method for hybrid QM/MM calculations has been described in detail elsewhere<sup>34,35</sup> and will only be reviewed here briefly without comparison to other QM/MM methods.

The energy,  $E_{\text{tot}}$ , for the combined system can be written as a sum of the energies of the QM and MM parts ( $E_{\text{QM}}$ ,  $E_{\text{MM}}$ ) and the interaction energy between them ( $E_{\text{QM/MM}}$ ):

$$E_{\text{tot}} = E_{\text{QM}} + E_{\text{MM}} + E_{\text{QM/MM}} \quad (1)$$

The QM energy is calculated by taking into account the polarization caused by the charge distribution of the MM environment. This perturbation is included in the Fock matrix via an additional one-electron term; for example, the  $i$ th electron interacts with  $n$  point charges  $q_j$  of the MM environment according to

$$\mathbf{F}_i^{\text{pert}} = - \sum_{j=1}^n q_j \frac{1}{r_{ij}} \quad (2)$$

The corresponding Fock matrix in the atomic orbital basis is given by

$$\mathbf{F}_{\mu\nu}^{\text{pert}} = -\sum_{j=1}^n q_j \left\langle \mu \left| \frac{1}{r_{ij}} \right| \nu \right\rangle \quad (3)$$

The electron–point charge interaction integrals are often treated like electron–core interaction integrals in semiempirical theory. It has been common practice since CNDO/2<sup>36</sup> to express these integrals as two electron integrals in which the point charge is considered as an *ss* charge distribution. Within the NDDO approximation,<sup>37</sup> the Fock matrix perturbation terms become

$$\mathbf{F}_{\mu\nu}^{\text{pert}} = \begin{cases} \sum_{j=1}^n q_j (\mu\nu|ss) & \mu, \nu \in A \\ 0 & \mu \in A, \nu \in B \end{cases} \quad (4)$$

where we have used the Mulliken notation with *A* and *B* being different QM centers. These two-electron integrals are computed by means of the multipole approximation.<sup>38</sup>

The MM energy is calculated without any back polarization from the QM part as a sum of different contributions for bond stretch, angle bend, etc. Our implementation utilizes either the AMBER<sup>39</sup> or the Tripos<sup>26</sup> force field functional forms and parameters.

The QM/MM interaction energy is calculated using four contributions (van der Waals, two electrostatic contributions, restraints):

$$E_{\text{QM/MM}} = E_{\text{vdw}} + E_{\text{nucl}} + E_{\text{elec}} + E_{\text{restr}} \quad (5)$$

The van der Waals interaction energy,  $E_{\text{vdw}}$ , is given by

$$E_{\text{vdw}} = \sum_{i=1}^m \sum_{j=1}^n D_{ij} \left[ \left( \frac{a_{ij}^0}{r_{ij}} \right)^{12} - \left( \frac{a_{ij}^0}{r_{ij}} \right)^6 \right] \quad (6)$$

where the index *i* runs over all *m* QM atoms, while *j* runs over all *n* MM atoms.  $a_{ij}^0$  is the sum of the van der Waals radii of atoms *i* and *j*.  $D_{ij}$  is the potential energy depth, determined as the geometric mean of the atom-type-dependent *D* values of atoms *i* and *j* given by Rappé et al.<sup>40</sup>

The electrostatic interaction energy consists of two contributions: the Coulomb interactions of the MM point charges,  $q_j$ , with the nuclei of the QM system,  $q_i^{\text{nucl}}$ , ( $E_{\text{nucl}}$ , calculated classically) and with the QM electron distribution ( $E_{\text{elec}}$ ):

$$E_{\text{nucl}} = \sum_{i=1}^m \sum_{j=1}^n \frac{q_j}{\epsilon_{\text{eff}}} \frac{q_i^{\text{nucl}}}{r_{ij}} \quad (7)$$

$$E_{\text{elec}} = \sum_{i=1}^m \sum_{j=1}^n \frac{q_j}{\epsilon_{\text{eff}}} \sum_{\mu, \nu \in i} P_{\mu\nu} (\mu\nu|ss) \quad (8)$$

where  $P_{\mu\nu}$  is a density matrix element and the two-electron integral  $(\mu\nu|ss)$  is subject to the NDDO approximation. Both contributions include an effective dielectric constant,  $\epsilon_{\text{eff}}$ , which may be taken as constant or distance dependent ( $\epsilon_{\text{eff}} = \epsilon_{\text{eff}}(r_{ij})$ ).

The last energy contribution to the QM/MM interaction energy takes into account restraints between the QM and MM

part that apply a harmonic penalty function to, for example, distances between QM and MM atoms:

$$E_{\text{restr}} = \sum_{i=1}^{n_{\text{restr}}} k_i (d_i - d_i^0)^2; \quad d = |r_i^{\text{QM}} - r_i^{\text{MM}}| \quad (9)$$

Thus, our QM/MM model is a kind of “electronic embedding” (model B) according to Thiel’s nomenclature.<sup>41</sup>

## Appendix B

**Evaluation of the AM1 Zinc Parameters for Multinuclear Complexes.** To investigate the suitability of the AM1 parameters for zinc for structures of the type considered here, 23 multinuclear zinc complexes from the Cambridge Crystallographic Data Centre (CCDC)<sup>42</sup> were optimized with AM1 and, for comparison, with PM3.<sup>43</sup> The complexes contain 26–204 atoms and 2–7  $\text{Zn}^{2+}$  ions. The metal centers are coordinated mostly by oxygen and nitrogen ligands, some by alkyl and aryl ligands. Three of the compounds contain halide ligands, and one contains a thio ligand.

With the exception of two complexes that contain inorganic ligands, the experimental geometries of the AM1-optimized structures are reproduced, although the symmetry is distorted in some cases and the metal–ligand distances are enlarged. However, 10 of the PM3-optimized structures dissociated completely during the optimization. The details of the validation are given in Tables A1–A4; the validation structures are available as supporting material.

Four of the compounds were also geometry-optimized with DMol<sup>3,32</sup> implemented in the program package Materials Studio.<sup>33</sup> The DNP (double numerical plus polarization)<sup>32</sup> basis set and the PW91<sup>31</sup> generalized gradient approximation functional were used (for details, see Table A4). The DMol<sup>3</sup>-optimized structures are closer to the X-ray geometries, but the magnitude of the rms deviations reflects those of the AM1-optimized structures. Only one compound has a significantly larger rms deviation, which is caused by a twist of phenyl

**TABLE A1: rms Deviations (heavy atoms only) in Å of the Multicenter Zinc Complexes from the CCDC to the X-ray Structures<sup>a</sup>**

	AM1 (21 compds)	PM3 (15 compds)
mean value	0.753	0.935
standard deviation	0.484	0.558
minimal deviation	0.140	0.308
maximal deviation	1.931	2.034

<sup>a</sup> Compounds that dissociated during the optimization were not taken into account (they are compounds 15 and 17 for AM1 and compounds 2, 6, 8, 12, and 14–18 for PM3).

**TABLE A2: Absolute Distance Deviations in Å of the AM1-Optimized Multicenter Zinc Complexes (taken from the CCDC) to the X-ray Structures<sup>a</sup>**

	$\text{Zn}^{2+}$ – $\text{Zn}^{2+}$ (53 atom pairs)	$\text{Zn}^{2+}$ –O (120 atom pairs)	$\text{Zn}^{2+}$ –N (48 atom pairs)
mean value	0.299	0.193	0.147
standard deviation	0.142	0.054	0.073
minimal deviation	0.096	0.062	0.014
maximal deviation	0.540	0.317	0.310

<sup>a</sup> All  $\text{Zn}^{2+}$ –ligand and the  $\text{Zn}^{2+}$ – $\text{Zn}^{2+}$  distances with the exception of those in compounds 3 and 9 are larger in the optimized structures. Compounds that dissociated during the optimization and those with an rms deviation greater 1 Å were not taken into account.



**TABLE A3: CCDC Codes, Number of Atoms, Number of  $\text{Zn}^{2+}$  Centers, Coordination Numbers of the  $\text{Zn}^{2+}$  Ions, and rms Deviations in Å of the AM1-Optimized Multicenter Zinc Complexes to the X-ray Structures**

no.	CCDC entry	number of atoms	number of $\text{Zn}^{2+}$	coord no.	rmsd [Å]	remarks
1	CACCEO10	74	2	4	0.864	interaction with methyl groups
2	FOFTUP	120	4	4/6	0.645	
3	TAGFOW	46	2	3	0.610	interaction with aryl carbon
4	ZIFSEM	126	2	5	0.789	
5	MZNMOX10	40	4	4	0.140	
6	NAMCAF	204	4	5	1.493	distorted
7	SUFBI	89	4	4	0.545	
8	ZNACAT10	87	3	5/6	0.679	
9	ZUWCUP	64	4	4	0.223	
10	CEATHZ	96	4	4	0.722	
11	CEPZAY	64	4	4	0.501	
12	CINHIQ	142	4	4/6	0.651	
13	COWHIF	103	3	4/6	1.392	change in coordination
14	DACPZN	101	7	4/6	0.989	change in coordination
15	DIFWEU10	26	2	4		dissociated
16	DUTVOD10	88	2	3	0.259	interaction with methyl groups
17	HEHRER	66	2	5/6		dissociated
18	JAMVIC	102	4	5/6	1.022	change in coordination
19	JAMYAX	82	2	4	0.237	
20	CADCEP	56	2	3	0.384	interaction with aryl hydrogen
21	FEEXAM	84	2	4	1.931	change in coordination
22	FUJXIR	68	2	4	0.186	
23	GIFZOK	43	3	2/3/5	1.557	

**TABLE A4: rms Deviations (Heavy Atoms Only) and Absolute Distance Deviations in Å of the DMol<sup>3</sup>-Optimized Complexes 3, 5, 11, and 20 to the X-ray Structures<sup>a</sup>**

DMol <sup>3</sup> rms Deviations		
no.	X-ray	AM1
3	0.483	0.824
5	0.108	0.068
11	0.324	0.313
20	0.105	0.359

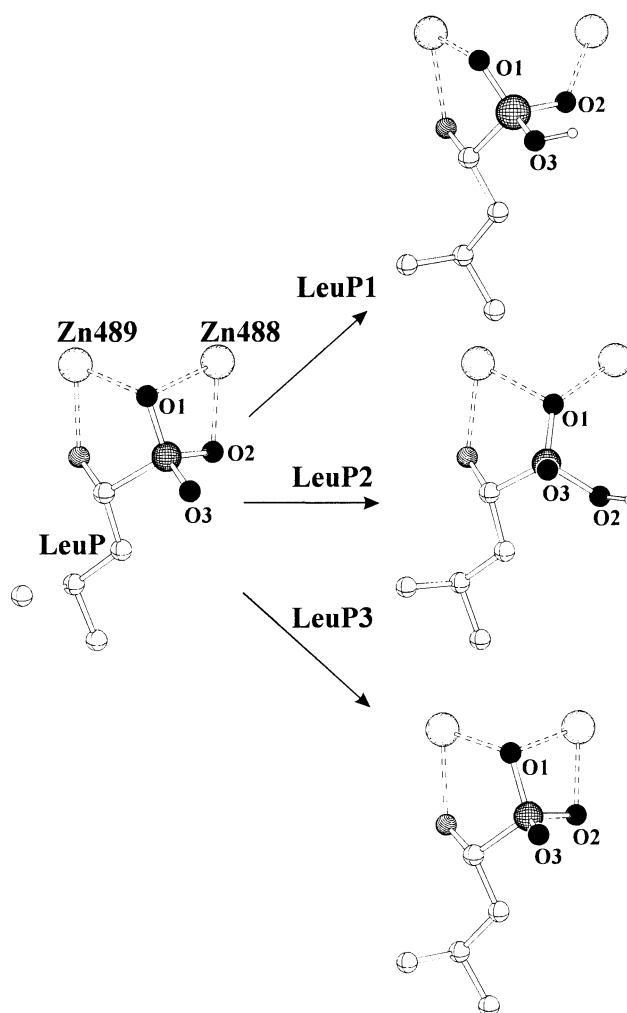
  

Distance Deviations			
	$\text{Zn}^{2+}-\text{Zn}^{2+}$ (14 atom pairs)	$\text{Zn}^{2+}-\text{O}$ (20 atom pairs)	$\text{Zn}^{2+}-\text{N}$ (8 atom pairs)
mean value	0.088 (0.257)	0.042 (0.195)	0.043 (0.190)
standard deviation	0.036 (0.076)	0.022 (0.076)	0.035 (0.092)
minimal deviation	0.011 (0.100)	0.000 (0.101)	0.014 (0.082)
maximal deviation	0.163 (0.379)	0.082 (0.310)	0.131 (0.310)

<sup>a</sup> The AM1 results for these compounds are given in brackets for comparison. For the rms deviations of the AM1-optimized results to the X-ray structures, see Table A3.

ligands. The  $\text{Zn}^{2+}-\text{Zn}^{2+}$  and  $\text{Zn}^{2+}-\text{ligand}$  distances correspond better to the X-ray structure, but like the AM1-optimized structures, they are larger. This suggests that the differences between the X-ray and the optimized geometries are caused partly by crystallization effects that are not taken into account by the gas-phase calculations.

Altogether, the geometries of the AM1-optimized complexes are reproduced well enough to make AM1 suitable for studying the reaction mode of bLAP. Because a single system is investigated, possible inaccuracies are compensated. In those cases in which CCDB compounds dissociated or the symmetry was lowered on optimization with AM1, either inorganic or very bulky ligands such as quinoline were involved. Such ligands are, however, not relevant for this investigation.

**Figure C1.** Geometry-optimized structures of the inhibitor L-leucine-phosphonate (LeuP) depending on the protonation pattern of the phosphonate group.

## Appendix C

**Optimization of the Free enzyme and the Enzyme–Inhibitor Complexes.** To investigate how well the experimental bLAP structures are reproduced by AM1, the free enzyme, containing a hydroxide ion or a water molecule, and the enzyme–inhibitor complex were geometry-optimized. The second  $\text{pK}_a$  of phosphonic acid is 6.7,<sup>44</sup> so that LeuP, which was used in the experiment, is probably deprotonated at pH 8. However, the total charge of the deprotonated inhibitor is  $-2$ ; the *gem*-diolate group of a tetrahedral intermediate has a charge of  $-1$ . A single protonated phosphonate group with a charge of  $-1$  therefore represents a better transition-state analogue. The proton can be positioned at O1, O2, or O3 of the phosphonate group with a resulting charge of  $-1$  (see Figure C1). However, a proton located between the two metal ions is unlikely. This leaves three systems to be studied: LeuP1 (protonated at O3), LeuP2 (protonated at O2), and LeuP3 (unprotonated). These structures are shown in Figure C1.

All systems were calculated with several different environments to study the influence of a possible bicarbonate ion located near the active site, as has been proposed in the literature.<sup>13</sup> Carbonic acid has a  $\text{pK}_a$  of 6.4<sup>45</sup> in water, but this can vary depending on the environment. Therefore, an equilibrium between carbonic acid and bicarbonate is possible and should be taken into account. Three different environments were there-

**TABLE C1: Some Relevant Distances in Å of the Geometry-Optimized Free Enzyme (CA Environment) Compared to the X-ray Structure (PDB Entry 1LAM)**

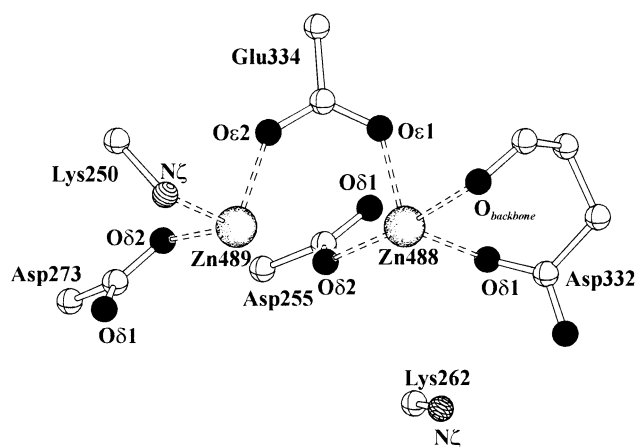
distance between	X-ray	optimized complex	
		hydroxide	water
Zn488–Zn489	3.02	3.31	3.74
Zn488–O <sub>hydroxide/water</sub>	2.01	2.10	4.22
Zn488–Asp255–Oδ1	3.25	3.27	2.26
Zn488–Asp255–Oδ2	2.12	2.10	2.23
Zn488–Asp332–Oδ1	1.98	2.12	2.02
Zn488–Asp332–O <sub>backbone</sub>	2.12	2.40	2.37
Zn488–Glu334–Oε1	2.02	2.13	2.12
Zn489–O <sub>hydroxide/water</sub>	1.95	2.07	2.26
Zn489–Lys250–Nζ	2.17	2.10	2.13
Zn489–Asp255–Oδ2	2.60	3.51	2.25
Zn489–Asp273–Oδ2	1.98	2.09	2.08
Zn489–Glu334–Oε2	2.02	2.17	2.13
Lys250–Nζ–Asp273–Oδ1	3.10	2.90	2.96
Asp255–Oδ2–Lys262–Nζ	3.93	2.95	4.14
Asp255–Oδ2–O <sub>hydroxide/water</sub>	2.80	2.83	2.83
Lys262–Nζ–Asp332–Oδ1	3.16	2.70	3.10
Lys262–Nζ–Asp332–Oδ2	2.89	2.90	3.29
Asp332–O <sub>backbone</sub> –Glu334–N <sub>backbone</sub>	3.17	3.19	3.10
Glu334–Oε1–Glu334–N <sub>backbone</sub>	3.07	2.98	3.06

fore used for the calculations, one containing a carbonic acid molecule (CA), one containing a bicarbonate ion (BIC), and one without (NOCA). Because the MM environment structures are not isomeric, the quantum mechanical energies including the van der Waals and Coulomb stabilization were used for energy comparisons.

**The Free Enzyme.** The structure of the hydroxide-containing system optimized in the CA-environment is most stable. The energy of the BIC system is 3.3 kcal mol<sup>−1</sup> higher and that of the NOCA system 2.7 kcal mol<sup>−1</sup>. The largest energy contribution is that of the van der Waals-QM/MM interaction energy. The geometries are very similar; the pure QM energies (without van der Waals and Coulomb stabilization) differ by less than 1 kcal mol<sup>−1</sup>, the rms deviations by less than 0.1 Å.

Table C1 gives some relevant distances of the optimized CA system compared to those found in the X-ray structure of the free enzyme (PDB entry 1LAM<sup>8</sup>). The coordination numbers of the Zn<sup>2+</sup> ions (5 for Zn488 and 4 for Zn489) are unchanged by the optimization; only the weak interaction between Zn489 and Asp255–Oδ2 is broken. Similar to the CCDC complexes studied (cf. Appendix B), the metal–metal distance and most of the metal–ligand distances are slightly larger in the optimized structures than those in the X-ray structure. One exception is the coordination distance between Zn489 and Lys250–Nζ, which is slightly shorter. The largest deviation of the metal coordination distances is between Zn488 and the backbone carbonyl oxygen of Asp332, which is 0.28 Å longer in the optimized system. However, this ligand is very weakly bound,<sup>7</sup> and its coordination distance varies in the different X-ray structures. In the enzyme–inhibitor complex 1LCP,<sup>10</sup> it is 2.19 Å, in the complex 1BLL<sup>9</sup> 2.37 Å. Taking into account that possible crystallization effects are missing and that the starting structure was derived from a different X-ray structure, the deviations are acceptable.

Lys262 is strongly involved in hydrogen bonds. The X-ray structure shows interactions with Asp332–Oδ1 and –Oδ2, although the distance from Lys262–Nζ to Oδ1 is 0.21 Å longer than that to Oδ2. The optimization indicates a stronger interaction to Oδ1. Furthermore, Lys262 forms a hydrogen bond to Asp255–Oδ2 in the optimized structure. As a result, the weak interaction between Zn489 and Asp255–Oδ2 is broken and the distance increases from 2.60 to 3.51 Å.

**Figure C2.** Relevant atom assignments of active-site components as used in the text.

The substitution of the hydroxide ion with a water molecule (to conserve the total charge of the system to allow an energy comparison, Lys262 was deprotonated) has the effect that the water molecule leaves the bridging position between the metal ions and becomes coordinated only to Zn489. This is accompanied by a change at Asp255, which is now a bidentate ligand to Zn488 and is additionally coordinated to Zn489 via Oδ2. Both Zn<sup>2+</sup> ions now have a coordination number of 5. Again, the CA system is the most stable and the QM/MM interaction energy has the largest contribution to the energy differences. Some distances are given in Table C1, the atom assignments are shown in Figure C2.

Apart from the changes in the water and Asp255 coordination, the substitution of the hydroxide ion has only a few effects. Because of the missing negatively charged bridging ligand, the metal–metal distance increases to 3.74 Å. The neutral Lys262 weakens its hydrogen bonds to Asp332, and the hydrogen bond to Asp255–Oδ2 is completely broken. The Zn489-coordinated water molecule now interacts with Asp273–Oδ1 (O–O distance 2.82 Å). The Zn489–O<sub>water</sub> distance is 2.26 Å.

**The LeuP Complexes.** The geometries of the optimized inhibitor systems depend on the protonation state of LeuP (Figure C1). LeuP1 (protonated at O3) is coordinated via O1 to Zn489 and via O2 to Zn488. Neither of the two oxygens is in a bridging position, and the distance between the two metal ions increases to 3.90 Å. LeuP2 (protonated at O2) is only coordinated via O1, which is located between the Zn<sup>2+</sup> ions. O2 forms a hydrogen bridge to Lys262–Nζ. The metal–metal distance, which is obviously strongly dependent on the presence of a bridging ligand, is 3.31 Å. Only LeuP3, which is not protonated, shows the same coordination pattern as that found in the X-ray structure—O1 is a bridging ligand and O2 is additionally coordinated to Zn488. The zinc–zinc distance is 3.26 Å. The coordination number for the two Zn<sup>2+</sup> ions is 5 in all systems. Some relevant distances are given in Table C2.

An obvious difference between the X-ray and the optimized structures is that Asp332–O<sub>backbone</sub> is not coordinated to Zn488. The oxygen moves away from the metal ion completely. This is accompanied by a twist of the backbone that allows a hydrogen bond between the backbone NH of Ala333 and the backbone carbonyl oxygen of Thr331 (which is included in the QM part as the N-terminal end of the peptide fragment Asp332–Glu334). In LeuP1 and LeuP2, Asp255–Oδ1 is also coordinated to Zn488, so the coordination number of the Zn<sup>2+</sup> ion is still 5. In LeuP3, two phosphonate oxygens are coordinated to Zn488 and there is no remaining vacant binding site.

**TABLE C2: Some Relevant Distances in Å of the Geometry-Optimized Inhibitor–Enzyme Complex (CA Environment) Compared to the X-ray Structure (PDB Entry 1LCP)**

distance between	X-ray	optimized complex		
		LeuP1	LeuP2	LeuP3
Zn488–Zn489	3.37	3.90	3.31	3.26
Zn488–O1 <sub>LeuP</sub>	2.49	3.60	2.18	2.19
Zn488–O2 <sub>LeuP</sub>	2.11	2.19	3.51	2.17
Zn488–Asp255–Oδ1	3.11	2.25	2.26	3.56
Zn488–Asp255–Oδ2	2.12	2.26	2.24	2.12
Zn488–Asp332–Oδ1	2.02	2.09	2.10	2.19
Zn488–Asp332–O <sub>backbone</sub>	2.19	4.29	4.37	4.63
Zn488–Glu334–Oε1	2.01	2.11	2.09	2.18
Zn489–O1 <sub>LeuP</sub>	2.25	2.16	2.29	2.12
Zn489–N <sub>LeuP</sub>	2.28	2.36	2.26	2.28
Zn489–Lys250–Nζ	2.12	2.07	2.12	2.12
Zn489–Asp255–Oδ2	2.70	3.62	3.34	3.68
Zn489–Asp273–Oδ2	2.12	2.15	2.14	2.19
Zn489–Glu334–Oε2	2.08	2.18	2.19	2.19
Lys250–Nζ–Asp273–Oδ1	3.03	2.94	2.93	2.94
Asp273–Oδ1–N <sub>LeuP</sub>	2.89	2.83	2.79	2.82
Asp255–Oδ2–Lys262–Nζ	3.72	3.01	3.00	2.97
Lys262–Nζ–Asp332–Oδ1	3.08	2.80	2.79	2.87
Lys262–Nζ–Asp332–Oδ2	2.87	2.85	2.77	2.75
Lys262–Nζ–O2 <sub>LeuP</sub>	2.68	3.07	2.82	2.76
Asp332–O <sub>backbone</sub> –Glu334–N <sub>backbone</sub>	3.21	4.44	4.47	4.72
Glu334–Oε1–Glu334–N <sub>backbone</sub>	2.98	2.97	2.95	2.96

The rms deviations (heavy atoms only) of the bILAP complexes with LeuP1, LeuP2, and LeuP3 relative to the X-ray structure are 0.375, 0.385, and 0.412 Å. Regarding the backbone atoms only, they are considerably smaller (0.230, 0.229, and 0.266 Å). Because of the movement of Asp332–O<sub>backbone</sub>, the fragment Asp332–Ala333–Glu334 has the highest contribution. The backbone atoms of the residues Lys250, Asp255, Lys260, and Asp273 give only a deviation of 0.146, 0.154, and 0.160 Å compared to the X-ray structure indicating that the QM/MM system separation approach induces no artificial distortion to the active-site geometry.

The above structures were obtained using the CA environment, which again gives the energetically most favorable results. The geometries obtained with the NOCA environment are nearly identical. However, in the presence of a bicarbonate ion, the Zn488–Asp332–O<sub>backbone</sub> coordination is not broken in all three systems. Moreover, both LeuP1 and LeuP3 have a 6-fold coordinated Zn488, although the coordination distances to Asp332–O<sub>backbone</sub> are very long (2.55 Å for LeuP1 and 2.46 Å for LeuP3). This effect is caused by the electrostatic influence of the bicarbonate, which can be shown by reducing the charges on the bicarbonate. Scaling factors of 0.75 for LeuP1 and 0.10 in the case of LeuP2 lead to a structure like the one obtained with the CA environment (the total charge of the MM part was compensated, cf. Computational Details). Substitution of the carbonic acid by three water molecules leads to the same result. On the other hand, variation of the dielectric constant has no effect on the geometry nor does the reduction of the van der Waals radii of the bicarbonate atoms in the MM part to 0.1 Å. In both cases, the Zn488–Asp332–O<sub>backbone</sub> coordination is preserved. There is no obvious explanation for this behavior. The structure of the active site seems to react very sensitively to variations in the charge distribution of the environment. The driving force of the coordination cleavage might be the conservation of the Zn488 coordination number, which prefers to be 5. The trend of the QM/MM interaction energy shows that the NOCA geometry is increasingly destabilized until the geometry change occurs. Beyond that point, the stabilization increases again.

To investigate whether the bicarbonate ion has a further effect on the geometry of the active site, calculations with the bicarbonate included in the QM part were performed. The bicarbonate remains more or less at the position it occupies in the MM part, but the 6-fold coordination of Zn488 in LeuP1 and LeuP3 changes. In LeuP1, Asp255–Oδ1 is no longer coordinated to Zn488; in LeuP3, the Asp332–O<sub>backbone</sub> coordination is broken. In both systems, the coordination number of Zn488 changes to 5.

With the exception of the changes in the Zn488 coordination, the quantum mechanically calculated structures are in good agreement with the X-ray structures. LeuP3 resembles the inhibitor as it exists in the X-ray structure 1LCP, although there the bridging oxygen O1 is coordinated more strongly to Zn489 than to Zn488. This indicates a tendency toward the LeuP1 coordination pattern. The optimized system LeuP3 shows a nearly symmetrically coordinated O1. The experimental results may possibly apply to an equilibrium between the singly protonated and deprotonated inhibitor. However, a clear result of the calculations on the hydroxide, water, and inhibitor systems is that the zinc–zinc distance increases considerably when no bridging ligand is present.

**Supporting Information Available:** The coordinates of the multinuclear zinc complexes in PDB format used for the validation of the zinc parameters (see Appendix B). This material is available free of charge via the Internet at <http://pubs.acs.org>.

## References and Notes

- (1) Review: Taylor, A. *FASEB J.* **1993**, *7*, 290–298.
- (2) Umezawa, H. *Recent Results Cancer Res.* **1980**, *40*, 115–125.
- (3) Taylor, A.; Daims, M. A.; Lee, J.; Surgenor, T. *Curr. Eye Res.* **1982**, *2*, 47–56.
- (4) Pulido-Cejudo, G.; Conway, B.; Proulx, P.; Brown, R.; Izaguirre, C. A. *Antiviral Res.* **1997**, *36*, 167–177.
- (5) Bernstein, F. C.; Koetzle, T. F.; Williams, G. J. B.; Meyer, E. F., Jr.; Brice, M. D.; Rodgers, J. R.; Kennard, O.; Shimanouchi, T.; Tasumi, M. *J. Mol. Biol.* **1977**, *112*, 535–542. URL <http://www.rcsb.org/pdb>.
- (6) Burley, S. K.; David, P. R.; Taylor, A.; Lipscomb, W. N. *Proc. Natl. Acad. Sci.* **1990**, *87*, 6878–6882.
- (7) Kim, H.; Lipscomb, W. N. *Proc. Natl. Acad. Sci.* **1993**, *90*, 5006–5010.
- (8) Sträter, N.; Lipscomb, W. N. *Biochemistry* **1995**, *34*, 14792–14800.
- (9) Kim, H.; Lipscomb, W. N. *Biochemistry* **1993**, *32*, 8465–8478.
- (10) Sträter, N.; Lipscomb, W. N. *Biochemistry* **1995**, *34*, 9200–9210.
- (11) (a) Review on binuclear metallohydrolases: Wilcox, D. E. *Chem. Rev.* **1996**, *96*, 2435–2458. (b) Review on zinc enzymology: Sträter, N.; Lipscomb, W. N. *Chem. Rev.* **1996**, *96*, 2375–2433.
- (12) (a) Grembecka, J.; Kedziński, P.; Sokalski, W. A. *Chem. Phys. Lett.* **1999**, *313*, 385–392. (b) Grembecka, J.; Sokalski, W. A.; Kafarski, P. *Int. J. Quantum Chem.* **2001**, *84*, 302–310.
- (13) Sträter, N.; Sun, L.; Kantrowitz, E. R.; Lipscomb, W. N. *Proc. Natl. Acad. Sci.* **1999**, *96*, 11151–11155.
- (14) Dugas, H. *Bioorganic Chemistry*, 3rd ed.; Springer-Verlag: New York, Berlin, Heidelberg, 1996; p 163.
- (15) Alex, A.; Clark, T. *J. Comput. Chem.* **1992**, *13*, 704–717.
- (16) von Onciul, A. R.; Clark, T. *J. Comput. Chem.* **1993**, *14*, 392–400.
- (17) Herz, T. Diploma Thesis, University of Erlangen-Nürnberg, Erlangen, Germany, 1996.
- (18) Hartmann, M.; Merz, K. M., Jr.; Eldik, R. v.; Clark, T. *J. Mol. Model.* **1998**, *4*, 355–365.
- (19) Some examples: (a) Schmidt, R. K.; Gready, J. E. *J. Mol. Struct. (THEOCHEM)* **2000**, *498*, 101–112. (b) Martí, S.; Andrés, J.; Moliner, V.; Silla, E.; Tuñón, I.; Bertrán, J. *J. Phys. Chem. B* **2000**, *104*, 11308–11315. (c) Titmuss, S. J.; Cummins, P. L.; Bliznyuk, A. A.; Rendell, A. P.; Gready, J. E. *Chem. Phys. Lett.* **2000**, *320*, 169–176. (d) Antonczaj, S.; Monard, G.; Ruiz-Lopez, M. F.; Rivail, J.-L. *J. Am. Chem. Soc.* **1998**, *120*, 8825–8833. (e) Hart, J. C.; Burton, N. A.; Hillier, I. H.; Harrison, M. J.; Jewsbury, P. *Chem. Commun.* **1997**, 1431–1432. (f) Cunningham, M. A.; Ho, L. L.; Nguyen, D. T.; Gillilan, R. E.; Bash, P. A. *Biochemistry* **1997**, *36*, 4800–4816. (g) Lyne, P. D.; Mulholland, A. J.; Richards, W. G. *J. Am. Chem. Soc.* **1995**, *117*, 11345–11350.

- (20) Schürer, G.; Lanig, H.; Clark, T. *J. Phys. Chem. B* **2000**, *104*, 1349–1361.
- (21) Clark, T.; Alex, A.; Beck, B.; Chandrasekhar, J.; Gedeck, P.; Horn, A.; Hutter, M.; Martin, B.; Rauhut, G.; Sauer, W.; Schindler, T.; Steinke, T. *Vamp 7.5 B18*; Erlangen-Nürnberg: Erlangen, Germany, 2001.
- (22) (a) Banerjee, A.; Adams, N.; Simons, J.; Shepard, R. *J. Phys. Chem.* **1985**, *89*, 52–57. (b) Baker, J. *J. Comput. Chem.* **1982**, *3*, 214–218.
- (23) (a) Liu, D. C.; Nocedal, J. *Math. Programming* **1985**, *45*, 503–528. (b) Nocedal, J. *Math. Comput.* **1980**, *24*, 773–782.
- (24) Gasteiger, J.; Marsili, M. *Tetrahedron* **1980**, *36*, 3219–3228.
- (25) *Sybyl 6.6*; Tripos Associates: St. Louis, MO, 1999.
- (26) Clark, M.; Cramer, R. D., III; Van Opdenbosch, N. *J. Comput. Chem.* **1989**, *10*, 982–1012.
- (27) Dewar, M. J. S.; Zoebisch, E. G.; Healy, E. F.; Stewart, J. J. P. *J. Am. Chem. Soc.* **1985**, *107*, 3902–3909.
- (28) Dewar, M. J. S.; Merz, K. M., Jr. *Organometallics* **1988**, *7*, 522–524.
- (29) Antonczak, S.; Ruiz-López, M.; Rivail, J.-L. *J. Mol. Model.* **1997**, *3*, 434–442.
- (30) Bertini, I.; Luchinat, C.; Rosi, M.; Sgamellotti, A.; Tarantelli, F. *Inorg. Chem.* **1990**, *29*, 1460–1463.
- (31) Perdew, J. P.; Wang, Y. *Phys. Rev. B*, **1992**, *45*, 13244–13249.
- (32) (a) Delley, B. *J. Chem. Phys.* **1992**, *92*, 508–517. (b) Delley, B. *J. Chem. Phys.* **2000**, *113*, 7756–7764.
- (33) *Materials Studio 2.0*; Accelrys Inc.: San Diego, CA, 2001.
- (34) Clark, T.; Alex, A.; Beck, B.; Gedeck, P.; Lanig, H. *J. Mol. Model.* **1999**, *5*, 1–7.
- (35) Gedeck, P. Unpublished results.
- (36) Pople, J. A.; Segal, G. A. *J. Chem. Phys.* **1966**, *44*, 3289–3296.
- (37) Pople, J. A.; Beveridge, D. L. *Approximate Molecular Orbital Theory*; McGraw-Hill: New York, 1970.
- (38) Dewar, M. G. S.; Thiel, W. *Theor. Chim. Acta* **1977**, *46*, 89–104.
- (39) Cornell, W. D.; Cieplak, P.; Bayly, C.; Gould, I. R.; Merz, K. M., Jr.; Ferguson, D. M.; Spellmeyer, D. C.; Fox, T.; Caldwell, J. W.; Kollman, P. A. *J. Am. Chem. Soc.* **1995**, *117*, 5179–5197.
- (40) Rappé, A. K.; Casewit, C. J.; Colwell, K. S.; Goddard, W. A., III; Skiff, W. M. *J. Am. Chem. Soc.* **1992**, *114*, 10024–10035.
- (41) Bakowies, D.; Thiel, W. *J. Phys. Chem.* **1996**, *100*, 10580–10594.
- (42) Allan, F. H.; Bellard, S.; Brice, M. D. Cartwright, B. A.; Doubleday, A.; Higgs, H.; Hummelink, T.; Hummelink-Peters, B. G.; Kennard, O.; Motherwell, W. D. S.; Rodgers, J. R.; Watson, D. G. *Acta Crystallogr., Sect. B* **1979**, *35*, 2331–2338.
- (43) (a) Stewart, J. J. P. *J. Comput. Chem.* **1989**, *10*, 209–220. (b) Stewart, J. J. P. *J. Comput. Chem.* **1991**, *12*, 320–341.
- (44) Holleman, A. F.; Wiberg, E. *Lehrbuch der Anorganischen Chemie*, 91.–100. Ausgabe; Walter de Gruyter: Berlin, 1985; p 651.
- (45) Holleman, A. F.; Wiberg, E. *Lehrbuch der Anorganischen Chemie*, 91.–100. Ausgabe; Walter de Gruyter: Berlin, 1985; p 719.